Catalysts **2015**, *5*, 1770-1796; doi:10.3390/catal5041770

OPEN ACCESS

catalysts

ISSN 2073-4344

www.mdpi.com/journal/catalysts

Article

Part I: A Comparative Thermal Aging Study on the Regenerability of Rh/Al_2O_3 and Rh/Ce_xO_y-ZrO_2 as Model Catalysts for Automotive Three Way Catalysts

Qinghe Zheng [1], Robert Farrauto [1,*], Michel Deeba [2] and Ioannis Valsamakis [1]

[1] Earth and Environmental Engineering Department, Columbia University, 500 West 120th Street, New York, NY 10027, USA; E-Mails: qz2178@columbia.edu (Q.Z.); ioannis.valsamakis@gmail.com (I.V.)

[2] BASF Corporation, Research and Development Center, 25 Middlesex Essex Tpke, Iselin, NJ 08830-0770, USA; E-Mail: michel.deeba@basf.com

* Author to whom correspondence should be addressed; E-Mail: rf2182@columbia.edu; Tel.: +1-212-854-6390.

Academic Editor: Jae-Soon Choi

Received: 3 August 2015 / Accepted: 9 October 2015 / Published: 23 October 2015

Abstract: The rhodium (Rh) component in automotive three way catalysts (TWC) experiences severe thermal deactivation during fuel shutoff, an engine mode (e.g., at downhill coasting) used for enhancing fuel economy. In a subsequent switch to a slightly fuel rich condition, *in situ* catalyst regeneration is accomplished by reduction with H_2 generated through steam reforming catalyzed by Rh^0 sites. The present work reports the effects of the two processes on the activity and properties of 0.5% Rh/Al_2O_3 and 0.5% Rh/Ce_xO_y-ZrO_2 (CZO) as model catalysts for Rh-TWC. A very brief introduction of three way catalysts and system considerations is also given. During simulated fuel shutoff, catalyst deactivation is accelerated with increasing aging temperature from 800 °C to 1050 °C. Rh on a CZO support experiences less deactivation and faster regeneration than Rh on Al_2O_3. Catalyst characterization techniques including BET surface area, CO chemisorption, TPR, and XPS measurements were applied to examine the roles of metal-support interactions in each catalyst system. For Rh/Al_2O_3, strong metal-support interactions with the formation of stable rhodium aluminate ($Rh(AlO_2)_y$) complex dominates in fuel shutoff, leading to more difficult catalyst regeneration. For Rh/CZO, Rh sites were partially oxidized to Rh_2O_3 and were relatively easy to be reduced to active Rh^0 during regeneration.

Keywords: automotive three way catalysts (TWC); Rh/Al_2O_3; Rh/Ce_xO_y-ZrO_2; fuel shutoff aging; catalyst deactivation; fuel rich regeneration; metal-support interaction

1. Introduction

When the gasoline engine is operated around the stoichiometric air-to-fuel ratio (14.6 wt.%, ±2%), a three way catalyst (TWC) allows simultaneous conversions (~98%) of CO, HCs and NO_x to innocuous compounds [1]. Specifically, the oxidation of CO and HCs (non-methane HCs) to CO_2 and steam (H_2O) is catalyzed by Pd, while NO_x is reduced to N_2 catalyzed by Rh [2]. Modern TWC uses supported bimetallic Pd-Rh catalysts deposited on stabilized γAl_2O_3 washcoated on a ceramic or metallic monolithic substrate [3–5]. A cartoon of a washcoated monolith is shown as Figure 1.

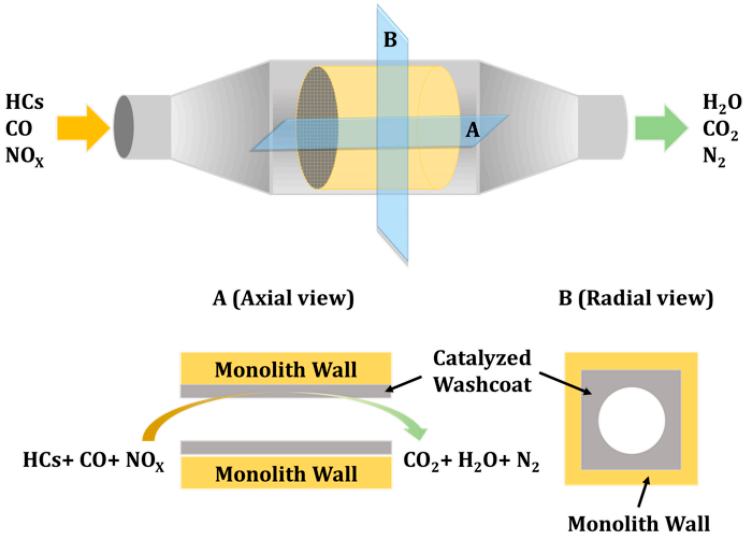

Figure 1. A washcoated monolith automotive TWC catalyst.

The TWC conversion profile is shown as Figure 2. CO and HCs are essentially fully oxidized at lean (excess O_2) of the stoichiometric air-to-fuel ratio (right side of stoichiometric). NO_x reduction occurs when little or no O_2 is present, as in the rich operating mode (left side of stoichiometric). The ratio of air-to-fuel in the exhaust to the air-to-fuel at stoichiometric is defined as the lambda point (λ). At stoichiometric operation, λ equals 1. The λ value is controlled via a feedback control system through a signal received from the O_2 sensor as shown in Figure 3.

Gamma-Al_2O_3 (γ-Al_2O_3), stabilized by incorporation of small percentages of La_2O_3 and/or BaO is most widely used as a support for the catalytic components due to its excellent hydrothermal stability, and high specific surface area and porosity, which provide adequate metal dispersion of the precious metals [6]. Cerium oxide (Ce_xO_y), well known for its high oxygen storage capacity (OSC) due to the function of Ce^{4+}/Ce^{3+} redox pair, is also included in modern TWC composition. The air-to-fuel ratio reversibly oscillates during lean/rich perturbations as a consequence of the feedback control strategy. The main function of the Ce_xO_y is to provide O_2 when $\lambda < 1$ for oxidation, and storing O_2 when $\lambda > 1$ to allow reduction to occur [2,7–9]. A schematic of the catalytic emission abatement system, with feedback

control, is shown in Figure 3. Note a small TWC converter close couple catalyst (next to the engine) gets hot faster than the main catalyst and initiates conversion more quickly. The O_2 sensor, after the main TWC, is for on-board diagnostics to inform the driver of a malfunction in the converter.

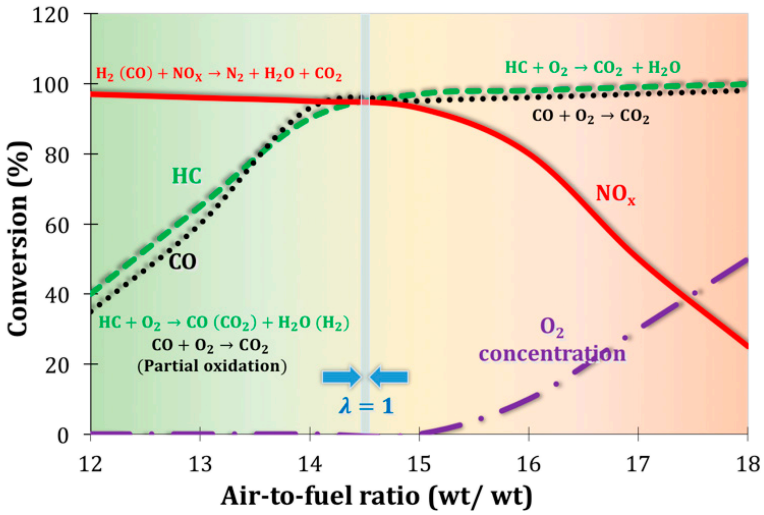

Figure 2. The TWC conversion profile as a function of air-to-fuel ratio.

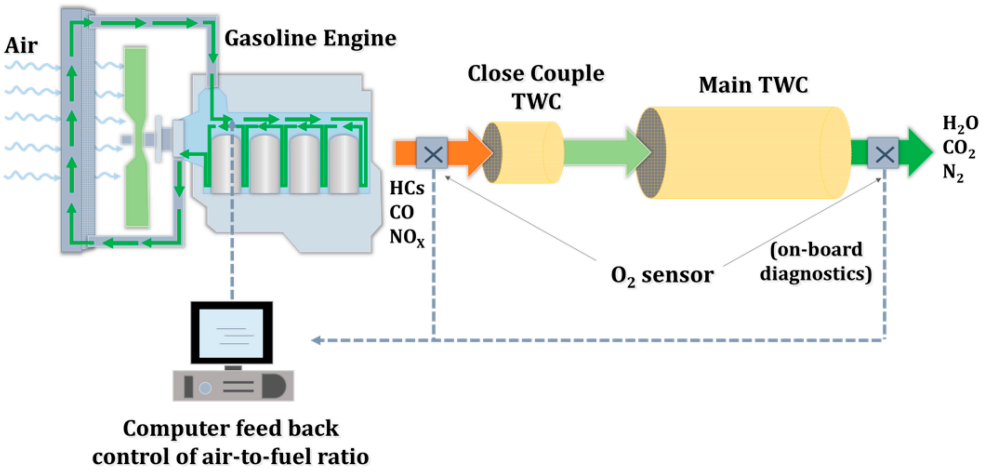

Figure 3. A schematic of the unit operations in the exhaust system for a TWC with feed back control of air-to-fuel ratio (λ).

The redox chemistry for the CeO_x is shown as Reactions (1) and (2). Further incorporation of zirconium oxide (ZrO_2) into Ce_xO_y crystallite structure (denoted as CZO) improves the thermal stability of Ce_xO_y, and enhances the mobility of lattice oxygen through the formation of oxygen vacancies [10–13]. Other proprietary elements are also added to further enhance performance.

$$2CeO_2 + CO \rightarrow Ce_2O_3 + CO_2 \text{ (at slightly fuel rich, } \lambda < 1) \quad (1)$$

$$Ce_2O_3 + \frac{1}{2}O_2 \rightarrow 2CeO_2 \text{ (at slightly fuel lean, } \lambda > 1) \quad (2)$$

Fuel shutoff has been practiced for many years for enhancing fuel economy by 2%–4%. This operational mode is implemented when the vehicle is coasting down hill, usually lasting a short period (no more than a few seconds or few minutes). During this operational mode, fuel injection is

discontinued and air flows into the TWC converter, exposing catalyst to high surface temperatures (up to 1050 °C), resulting in severe catalyst deactivation [14–16].

Rhodium needs to be maintained in its metallic state (Rh^0) to maintain its activity for NO_x reduction [2,17]. The deactivation modes include metal and/or support sintering [18,19], metal and/or support oxidation [20], and metal-support interactions [19–23]. It is widely accepted that the interaction between Rh and γ-Al_2O_3 during thermal oxidative exposure leads to the formation of stable and inactive Rhodium Aluminate $Rh(AlO_2)_y$ (Reaction 3) [2,17].

$$Rh_2O_3 + yAl_2O_3 + \frac{y-3}{2}O_2 \xrightarrow{800°C,air} 2\,Rh(AlO_2)_y \quad (3)$$

Interactions between Rh and Ce_xO_y in combination with ZrO_2 have been discussed previously. High surface energy of Ce_xO_y favors metal-support interactions. The dissolution of Rh into the bulk ceria was observed after catalyst calcination at 550 °C [24,25]. Meanwhile, Rh^+−O−Ce and $[Rh{-}O_2]^{2-}$ species are likely formed in an oxidative environment [26–29]. At high temperature, treatment of Rh/CeO_2 in air leads to the formation of Rh_2O_3 [30], slight Rh metal sintering [31,32], and segregation of Rh cations into the CeO_2 lattice [33,34]. Rh may also incorporate into the sublattice ZrO_2, leading to decrease in metal redox behavior [35].

Two practical approaches have been employed to solve (or partially solve) the deactivation problem: (1) stabilizing the support by using/adding refractory materials to prevent negative Rh-support interactions; and (2) regenerating the deactivated catalyst after fuel shutoff by operating engine at the fuel rich (λ < 1) condition [2,15,36–42]. For the first approach, refractory materials as supports in place of gamma Al_2O_3 include zirconia, titania, denser forms of alumina, and alkaline metal oxides [43,44] have been suggested. The second approach returns the operational mode to slightly fuel rich at ~500 °C, which allows the creation of a reducing engine exhaust atmosphere for partially reversing catalyst deactivation [2,45].

At slightly fuel rich conditions, the O_2 concentration is very low while considerable amounts of HCs and CO, along with excess steam and CO_2, are present in the exhaust. The oxidized catalytic components can be reduced by H_2 generated mainly through catalytic steam reforming (SR). The SR reaction, with propane as a model compound for the exhaust HC being reformed, is shown in Reaction (4) [46,47]. Fuel rich regeneration allows Rh^{3+} to be reduced to active Rh^0, and released from the interaction with the support. Reaction (5) represents the reverse of Rh-Al_2O_3 interaction by H_2. It is also possible for some dry reforming to occur where H_2O is replaced with CO_2.

$$C_3H_8 + 3H_2O \rightarrow 3CO + 7H_2 \quad (4)$$

$$2Rh(AlO_2)_y + yH_2 \xrightarrow{\text{Fuel rich}} 2Rh + yAl_2O_3 + yH_2O \quad (5)$$

One advantage of this process is that the endothermic SR reaction (which is both thermodynamcially and kinetically favorable at high temperature) can be catalyzed by the TWC catalyst itself. In other words, the deactivated components in TWC can be regenerated *in situ* by the H_2 produced through SR, as catalyzed by the precious metal sites (mainly Rh) remaining active after aging.

The present work shows new data of the effects of fuel shutoff and subsequent regeneration on the catalytic performance and properties of Rh-TWC, with 0.5% Rh/Al_2O_3 and 0.5% Rh/Ce_xO_y-ZrO_2 (Ce:Zr atomic ratio of 1:2) as model catalysts. Fuel shutoff was simulated by aging fresh catalysts in

flowing air at high temprature (800 °C, 950 °C, or 1050 °C) for a short period (5 min), while catalyst regeneration was performed by exposing the aged catalysts to a reducing atmosphere (500 vppm propane, 10% steam, 8% CO_2, and N_2 balance at 550 °C for 1 h), simulating a slightly rich exhaust composition which is close to normal engine operation. Catalyst regenerability was examined by comparing the activity of fresh, aged, and regenerated catalysts via H_2 generation. By combining various characterization techniques including BET, CO chemisorption, TPR, and XPS, the roles of catalyst properties were examined. The study (i) provides a mechanism study of catalyst deactivation during simulated fuel shutoff process; and (ii) explores the aging and support effects on catalyst regenerability during simulated fuel rich operation. The paper highlights the maintenance of catalyst performance through cyclic fuel shutoff-fuel rich operation.

2. Results and Discussions

2.1. Thermodynamic Model for TWC Conversion at Simulated Engine Fuel Rich Condition

The main reaction pathways occurring during fuel rich operation are listed in Table 1. Specifically, endothermic steam reforming of propane reactions (Reactions a and b) are thermodynamically and kinetically favorable at high temperature. Exothermic water gas shift (Reaction c) and methanation of CO_2 (Reaction d) reactions are thermodynamically favorable at relative low temperature, where reaction kinetics are slow. The CH_4 produced undergoes steam reforming (Reaction e). The reaction thermodynamics and kinetics are also largely dependent on the feed. When 8 vol-% CO_2 is considered (as present in the exhaust), it can react with CH_4 in what is referred to dry reforming.

Table 1. Main reaction pathways during catalytic conversions of simulated exhaust feed at fuel rich condition.

Reaction #	Reaction Pathways	Reaction Type (Forward Direction)	ΔH_r^0 (298 K) (kJ/mol)
a	$C_3H_8 + 3H_2O \rightarrow 3CO + 7H_2$	Propane steam reforming	+497.70
b	$C_3H_8 + 6H_2O \rightarrow 3CO_2 + 10H_2$	Propane steam reforming	+374.29
c	$CO + H_2O \rightleftharpoons CO_2 + H_2$	Water gas shift	−41.14
d	$CO_2 + 4H_2 \rightleftharpoons CH_4 + 2H_2O$	Methanation of CO_2	−165.02
e	$CH_4 + H_2O \rightleftharpoons CO + 3H_2$	Methane steam reforming	+206.16

The Gibbs free energy for main reactions (Reactions a–e) are plotted in Figure 4. The extent of methanation of CO_2 (Reaction d) and reverse water gas shift (reverse of Reaction c) increase in the presence of 8 vol-% CO_2 in the feed. Both of these reactions decrease H_2 content. It is clear SR is favored above about 450 °C.

Figure 5 shows the main equilibrium products (H_2, CO, and CH_4) and reactant (propane and water) equilibrium mole fractions at fuel rich condition (500 vppm propane, 10 vol-% steam, 8 vol-% CO_2, N_2 in balance). In the low temperature regime (T < 350 °C), steam reforming, water gas shift, and methanation reactions dominate. In the high temperature regime (T > 350 °C), WGS and methanation reactions become less favorable.

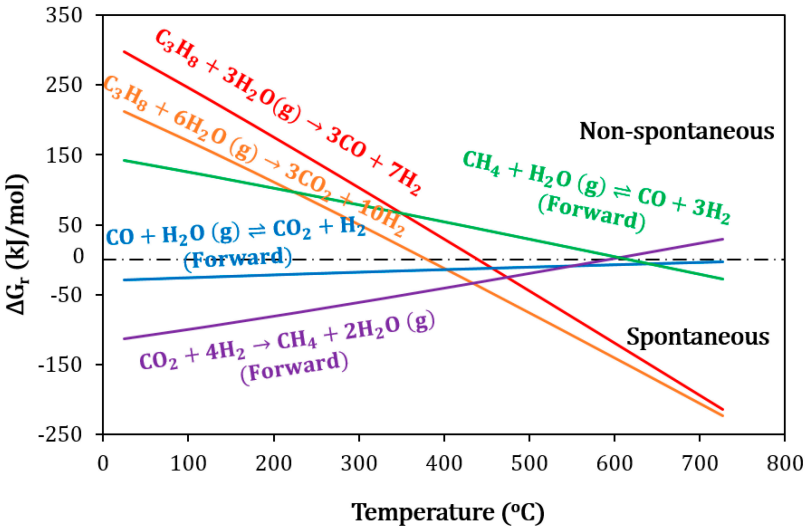

Figure 4. Reaction Gibbs free energy as a function of reaction temperature (25 °C to 700 °C) at 1 atm. Assume ideal gas behavior for the reactant and product gas components. Compound thermodynamic data with temperature and pressure inputs is collected from I. Barin, Thermochemical Data of Pure Substances (3rd Edition) [48].

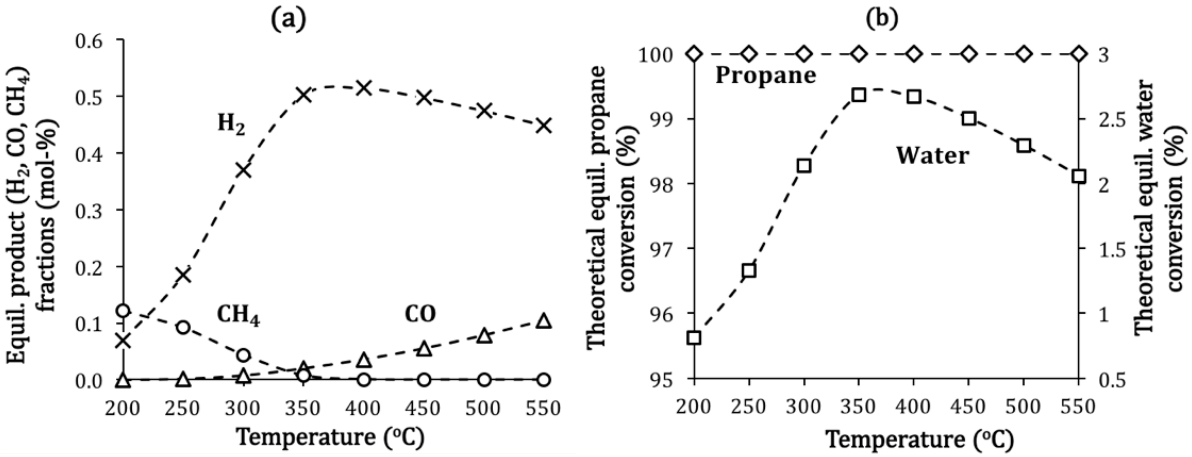

Figure 5. (**a**) Main mole fractions of H_2, CO, and CH_4; and (**b**) theoretical reactant (propane and water) conversions as a function of reaction temperature (200 °C to 550 °C) at thermodynamic equilibrium conditions. Reactant feed: 500 vppm propane, 10 vol-% steam, 8 vol-% CO_2, N_2 in balance.

2.2. Catalyst Deactivation and Regeneration

After aging in air at three temperatures (800 °C, 950 °C, or 1050 °C), the activity of fresh and aged Rh/Al_2O_3 and Rh/CZO are compared as the H_2 mole fraction in the propane rich feed gas (Figure 6). Fresh Rh/CZO (b) shows higher activity than Rh/Al_2O_3 (a) under fresh and all aged conditions.

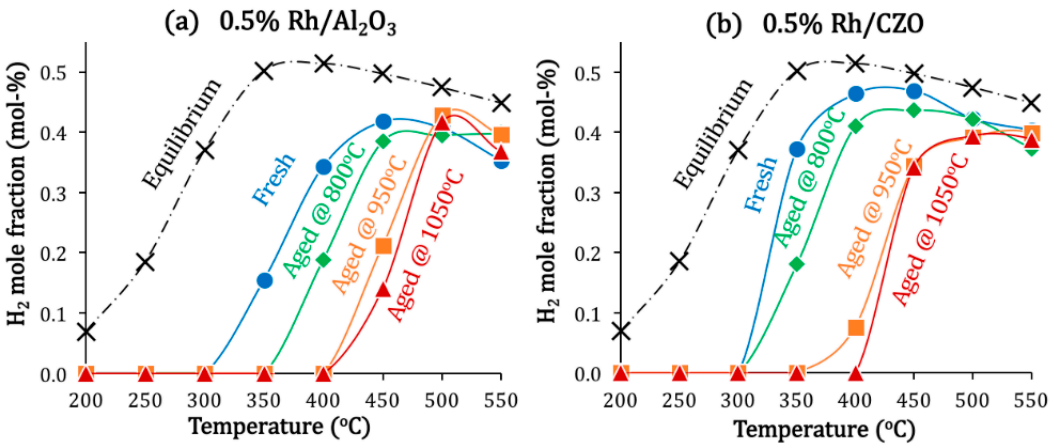

Figure 6. Catalyst activity of fresh and aged (**a**) 0.5% Rh/Al_2O_3 and (**b**) 0.5% Rh/CZO Catalyst activity is plotted in terms of H_2 mole fraction as a function of reaction temperature (200 °C–550 °C).

Not surprisingly, deactivation of both catalysts increases with aging temperature from 800 °C to 1050 °C. The most difficult regeneration was expected after aging at elevated temperatures. This is in agreement with a previous report [49]. Compared to Rh/Al_2O_3, fresh and aged Rh/CZO showed higher catalytic activity in converting propane to H_2.

The activity of fresh, aged, and regenerated catalysts are compared in Figure 7. The regeneration method was very effective in recovering full activity of Rh catalysts. This is also shown in Table 2, which compares the T_{50} of regenerated catalysts with those of fresh and aged. T_{50} is the temperature at which 50% maximum equilibrium H_2 production is achieved. The temperatures of Rh/CZO were always 40 °C lower than Rh/Al_2O_3, indicating a more rapid response to *in situ* regeneration.

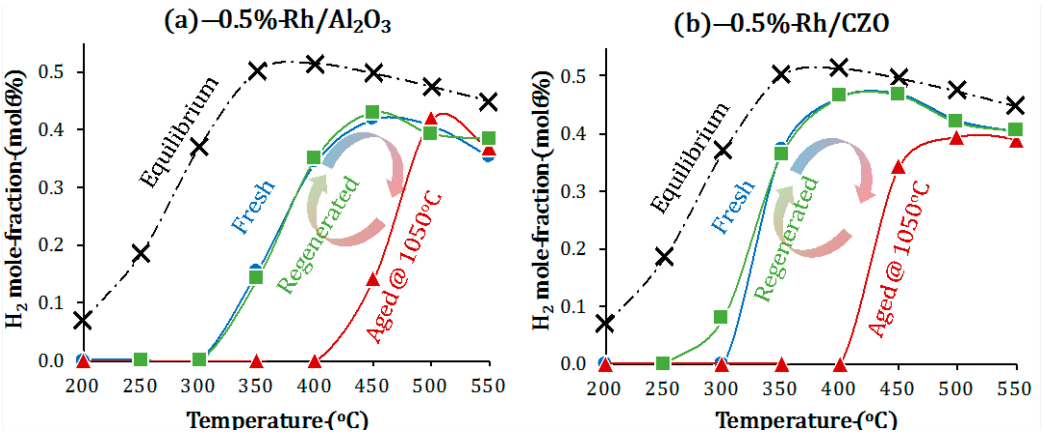

Figure 7. Activity of fresh, aged, and regenerated (**a**) 0.5% Rh/Al_2O_3 and (**b**) 0.5% Rh/CZO in converting simulated engine exhaust gas at fuel rich condition. Catalyst activity is plotted in terms of H_2 product mole fraction as a function of reaction temperature (200 °C to 550 °C). Aged catalysts were obtained by treating fresh ones in air at 1050 °C for 5 min, followed by cooling to room temperature in air. Catalyst regenerations were performed by at rich condition at 550 °C for 1 h.

Table 2. T_{50} (temperature at which 50% maximum equilibrium H_2 production is reached during activity tests, °C) of fresh, aged, and regenerated catalysts.

Catalyst	T_{50} (°C)				
	Fresh	After Aging in air for 5 min at Different temp.			After Regeneration *
		800 °C	950 °C	1050 °C	
0.5% Rh/Al_2O_3	375	415	460	470	375
0.5% Rh/CZO	334	365	431	435	330

* Catalyst regenerations were performed at 550 °C in propane-containing feed gas.

2.3. Catalyst Stability during Simulated Fuel Shutoff Aging-Fuel Rich Regeneration Cycle Tests

Figure 8 shows the rapid response (increased slope of H_2 production) achieved during regeneration for the Rh/CZO catalyst relative to the slower recovery of Rh/Al_2O_3.

The activity of both catalysts after every 5 cycles of aging-regeneration cycles are plotted in Figure 9. Significant losses of catalyst activity were observed in the first 5 cycles. The initial deactivations (greater for the Rh/Al_2O_3) are believed caused by Rh metal sintering and dissolution of oxidized Rh into the sintered support materials (metal-support interactions). After the first 5 cycles, the performance stabilized. At this condition the major deactivation modes have been completed and no further permanent deactivation is noted after repeated cycles. The aged catalysts could then be regenerated but to a lesser extent than after 5 cycles.

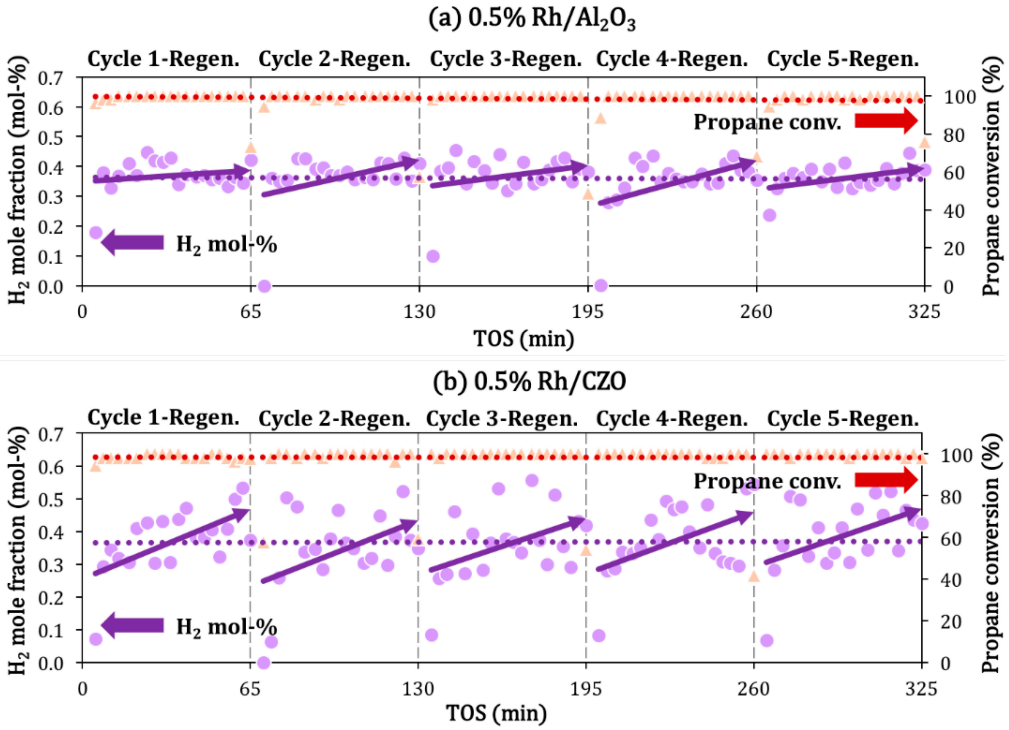

Figure 8. H_2 generations during regeneration processes in simulated fuel shutoff aging- fuel rich regeneration cycle tests (First 5 cycles out of total 25 cycles) with (**a**) 0.5% Rh/Al_2O_3 and (**b**) 0.5% Rh/CZO. In each cycle, the catalyst sample was first aged in air at 1050 °C for 5 min, followed by *in situ* regeneration at propane rich condition at 550 °C for 1 h.

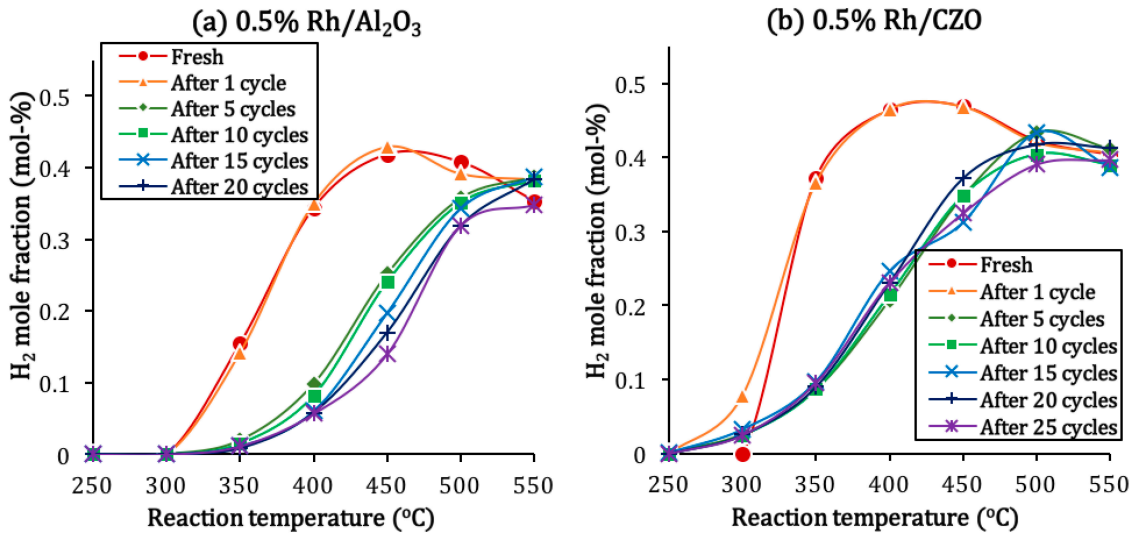

Figure 9. Activity of regenerated (**a**) 0.5% Rh/Al_2O_3 and (**b**) 0.5% Rh/CZO catalysts after 1, 5, 10, 15, 20, and 25 cycles in the aging-regeneration cycle tests. After every five cycles of aging/regeneration. The catalyst activity is plotted in terms of H_2 product mole fraction as a function of SR temperature from 250 °C to 550 °C.

2.4. Catalyst Deactivation and Regeneration Mechanisms

Figure 10 shows the BET surface areas of fresh and aged 0.5% Rh/Al_2O_3 and 0.5% Rh/CZO at different aging treatments. In agreement with the catalyst activity result as shown in Figure 6, most significant losses in catalyst surface areas occurred at 950 °C and 1050 °C. The Al_2O_3 support exhibited higher intrinsic surface area, but a slightly higher percentage of sintering relative to the CZO support (with 41.4% and 35.9% for Rh/Al_2O_3 and Rh/CZO respectively after 1050 °C aging). ZrO_2 in CZO support is likely the main contributor to the thermostability of Rh/CZO [50].

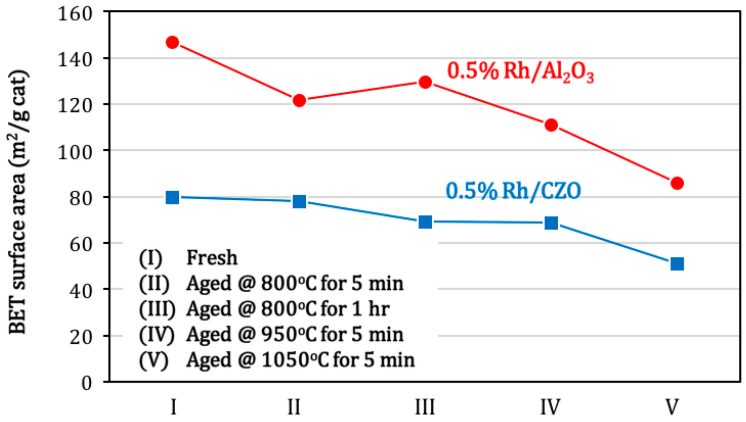

Figure 10. BET surface areas of fresh and aged (**a**) 0.5% Rh/Al_2O_3 and (**b**) 0.5% Rh/CZO, as a function of aging conditions. Aged samples were obtained by aging fresh catalysts (I) in air at the following conditions: (II) 800 °C for 5 min; (III) 800 °C for 1 h; (IV) 950 °C for 5 min; or (V) 1050 °C for 5 min. The aging processes were followed by cooling in air to room temperature. As a reference, BET surface areas of support materials were measured 142.9 m^2/g and 60.3 m^2/g respectively for fresh Al_2O_3 and CZO.

The metal dispersions of fresh and aged catalysts are shown in Table 3. Fresh Rh catalysts showed higher metal dispersions on CZO than on Al_2O_3. Soria and Duarte *et al.* [51,52] reported that the enhancement of metal dispersion in Rh/CeO_2 system was achieved by the Rh-Ce interaction (ceria stabilized Rh^+ species formed on the support). The higher metal dispersions likely enhance its activity in catalytic steam reforming of propane. After aging, loss of active metal sites occurs for both Rh catalysts, and is accelerated with increasing aging temperature from 800 °C to 1050 °C. Barbier *et al.* [53], reported that the decrease of Rh surface area in Rh/Al_2O_3 system was mainly linked to the diffusion of Rh^{3+} into the alumina matrix, while the presence of Ce_xO_y stabilizes Rh and prevents Rh^{3+} from dissolving into the support.

Table 3. Metal dispersions (%) of fresh and aged 0.5% Rh/Al_2O_3 and 0.5% Rh/CZO catalysts as measured by room temperature CO chemisorption [a]. After simulated fuel shutoff, loss of active metal sites occurred for both Rh catalysts, and was accelerated with aging temperature from 800 °C to 1050 °C.

Catalyst	Metal Dispersion (%)		
	Fresh	Aged @ 800 °C	Aged @ 1050 °C
$0.5\%Rh/Al_2O_3$	30.1	15.8	8.0
0.5%Rh/CZO	80.7	40.2	27.9

[a] CO can only be chemisorbed on Rh^0 in Rh/Al_2O_3 and Rh/CZO. CO chemisorption was negligible on non-reduced catalyst samples, and was zero on Al_2O_3 and CZO support-only material.

However, there likely exists an overestimation of the metal particle dispersion by measuring the CO chemisorption of Rh/CZO, due to the formation of carbonate species on CeO_2 surface even at low temperature (323 K) and by the likelihood of multiple CO molecules adsorbing on the Rh itself. Some preliminary TEM result as below (Table 4). After aging and regeneration, negligible metal crystallite size grow was observed with both Rh/Al_2O_3 and Rh/CZO, which supports our result that metal sintering was not the major deactivation mode in Rh-TWC. The dramatically reduced CO chemisorption capacity of the aged Rh-TWC together with the TEM images suggests that the main deactivation mode during 1050 °C aging was metal-support interaction.

Table 4. Mean metal particle sizes (nm) of fresh and aged TWCs as measured using TEM images.

Catalyst	Active Particle Mean Size (nm) *		
	Fresh	After Air Aging @ 1050 °C	After Regeneration
0.5% Rh/Al_2O_3	4.4	5.7	5.4
0.5% Rh/CZO	8.5	9.2	9.3

***** Feret diameter of active metal/metal oxide particle.

During air aging, the oxidation state of Rh increased in both Rh/Al_2O_3 and Rh/CZO, *i.e.*, $Rh^0 \rightarrow Rh^{3+}$ (Reaction 6). Meanwhile, strong metal-support interactions with the formation of Rhodium Aluminate ($Rh(AlO_2)_y$) took place in Rh/Al_2O_3 sample (Reaction 3) [50].

$$2Rh^0 + \frac{3}{2}O_2 \xrightarrow{>800℃} Rh_2O_3 \quad (6)$$

$$Rh_2O_3 + yAl_2O_3 + \frac{y-3}{2}O_2 \xrightarrow{800°C,air} 2\,Rh(AlO_2)_y \quad (3)$$

H_2-TPR was used to study the catalyst redox property after aging at different conditions (Figure 11). The lower the temperature of the H_2 consumption peak, the easier the reduction. The reductions of Rh^{3+} to Rh^0 in both catalysts occurred around 100 °C. H_2 reaction pathways on Rh sites include H_2 spill over and dissociation on Rh^0 sites (Reaction 7), and subsequent reduction of $Rh^{3+} \rightarrow Rh^0$ (Reaction 8) [54–56].

$$Rh^0 + \frac{x}{2}H_2 \rightleftharpoons Rh\cdots H_x \quad (7)$$

$$Rh_2O_3 + 6H \rightarrow 2Rh^0 + 3H_2O \quad (8)$$

Since Al_2O_3 is non-reducible, H_2 consumption peaks in fresh and aged Rh/Al_2O_3 are only assigned to Rh reductions. The results indicate that Rh in fresh Rh/Al_2O_3 was already partially oxidized with a H_2 consumption peak at 90 °C. After aging in air with (800–1050 °C), the TPR profiles of Rh/Al_2O_3 samples shifted to higher reducing temperatures, while the H_2 consumption peak area continued to increase. Rh was "released" from metal-support interaction by H_2 (Reaction 5), but this became increasingly difficult at higher aging temperature.

$$2Rh(AlO_2)_y + yH_2 \xrightarrow{\text{Fuel rich}} 2Rh + yAl_2O_3 + yH_2O \quad (5)$$

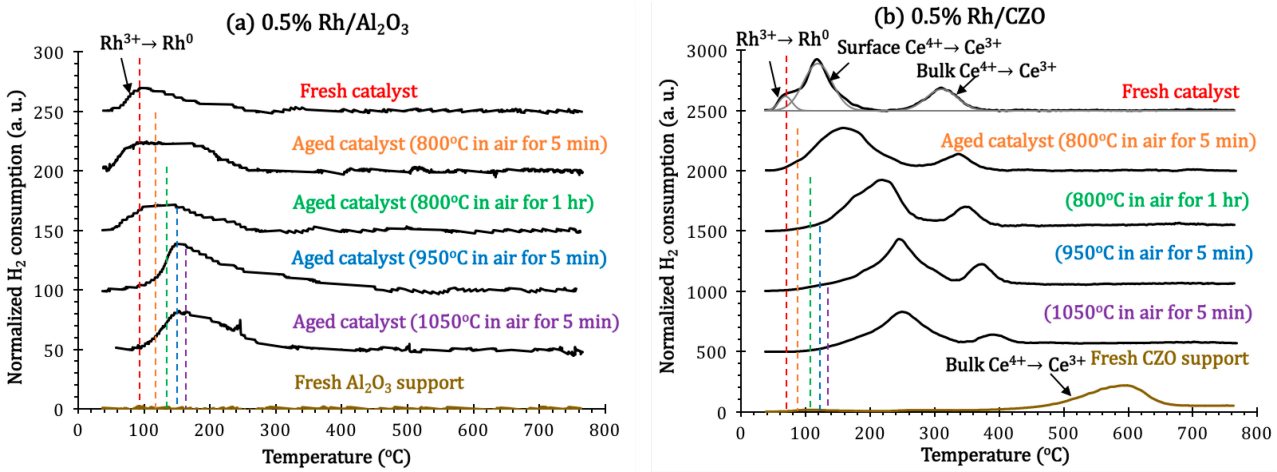

Figure 11. Normalized H_2 consumption in H_2-Temperature Programmed Reduction (H_2-TPR) measurements of fresh and aged (**a**) 0.5% Rh/Al_2O_3 and (**b**) 0.5% Rh/CZO, as a function of reducing temperature. Aged samples for measurements were respectively achieved by aging the fresh ones in air at the following conditions: 800 °C for 5 min, 800 °C for 1 h, 950 °C for 5 min, or 1050 °C for 5 min.

The precise stoichiometry of Rh:O is dependent on many factors including metal loading, metal dispersion, aging temperature, and aging oxygen partial pressure. Hwang *et al.* [50], reported the phase diagram for the variation of rhodium oxide species on the dispersion of rhodium samples and the oxidation temperature.

The quantitative H_2 consumption for the fresh and aged 0.5% Rh/Al_2O_3 samples during H_2-TPR is shown in Table 5. The H_2 consumptions correspond well to our statement that the fresh 0.5% Rh/Al_2O_3

sample was already partially oxidized. $N(H_2)/N(Rh)$, *i.e.*, the ratio between consumed H_2 molecules and reduced Rh atoms, increases with increasing aging temperature, and approaches 1.5 after high temperature (950 °C) aging, suggesting almost complete oxidation of Rh^0 to Rh^{3+} in severely aged 0.5% Rh/Al_2O_3. The H_2 consumption by rhodium oxides in 0.5% Rh/CZO is very difficult to quantify because the reduction of Ce^{4+} to Ce^{3+} also consumes H_2. For 0.5% Rh/CZO samples, qualitative TPR analysis and semi-quantitative XPS analysis (later text) are sufficient for the Rh oxidation state study.

Table 5. Reduction temperature (T_R) and H_2 consumption during H_2-TPR for fresh and aged 0.5% Rh/Al_2O_3 samples.

Sample	T_R (°C)	H_2 Consumption (μmol H_2/gcat)	$N(H_2)/N$ (Rh)
Fresh	90	31.78	0.65
Aged @ 800 °C for 5 min	118	59.78	1.23
Aged @ 800 °C for 1 h	135	72.85	1.50
Aged @ 950 °C for 5 min	150	70.49	1.45
Aged @ 1050 °C for 5 min	162	71.57	1.47

For fresh CZO support, one broad reduction peak is shown at 400–660 °C, which is assigned to bulk surface Ce^{4+} to Ce^{3+}, with the following global reaction (Reaction 9) [57–59].

$$2CeO_2 + H_2 \rightarrow Ce_2O_3 + H_2O \quad (9)$$

The reduction of Rh^{3+} to Rh^0 on CZO (71 °C) is easier than for fresh Rh/Al_2O_3 (91 °C). The presence of Rh in fresh Rh/CZO allows the reduction of Ce^{4+} to Ce^{3+} to occur at a lower temperature (100–420 °C), with the Ce^{4+} reduction peak split into two side peaks (at 110 °C and 308 °C respectively). The lower reduction temperature of Ce^{4+} (at 110 °C) occurs following the surface reduction of Rh^{3+}, suggesting that the Ce^{4+} sites being reduced were most likely the ones in close contact with the Rh sites. It has been reported that the redox properties of both Rh and Ce are enhanced when Rh is deposited on Ce_xO_y [60]. The Rh–O–Ce bond is likely formed, creating $Rh^{\delta+}/Rh^0$ ($0 < \delta < 1$) and Ce^{4+}/Ce^{3+} redox couple. Electrons transfer more efficiently during H_2 reduction [61–63]. The introduction of Zr into the Ce_xO_y crystal lattice, now widely practiced for OSC, stabilizes the Rh–Ce interaction via improving mobility of oxygen in Ce_xO_y or maintaining Ce_xO_y dispersion in nanometer scale [64–71]. Furthermore, the Rh–O–Ce bond can be very easily dissociated [60], which makes the interaction between Rh and Ce_xO_y much weaker than that between Rh and Al_2O_3. After complete reduction of $Rh^{\delta+}$ to Rh^0, electrons transfer from dissociated H_2 on Rh^0, allowing easier reduction of the bulk Ce^{4+} to Ce^{3+}. The schematic mechanism of the redox reaction pathways and the promotional metal-support interaction within 0.5% Rh/CZO during H_2-TPR are sketched in Figure 12.

In agreement with previous literature [72], increasing the aging temperature, the reduction of both Rh and Ce in Rh/CZO shifted to higher temperature values, suggesting decreases in hydrogen dissociation capability after aging.

The XPS Rh 3d electron orbitals were used to identify and semi-quantify the Rh oxidation states, by comparing the binding energy values and relative ratio of the corresponding states. Figure 13 profiles the XPS Rh 3d spectra of both catalysts, and Table 6 summarizes the peak information details. Rh $3d_{3/2}$ and Rh $3d_{5/2}$ peaks, resulting from spin-orbital splitting, with different binding energies (BE) corresponding to the Rh valence states were assigned [73–80]. For a fresh sample, Rh $3d_{5/2}$ peak with BE

of at 307.5 eV–308.4 eV is attributed to Rh^0 valence state, while Rh $3d_{5/2}$ peak at 309.2 eV–310.1 eV is attributed to Rh^{3+} valence state.

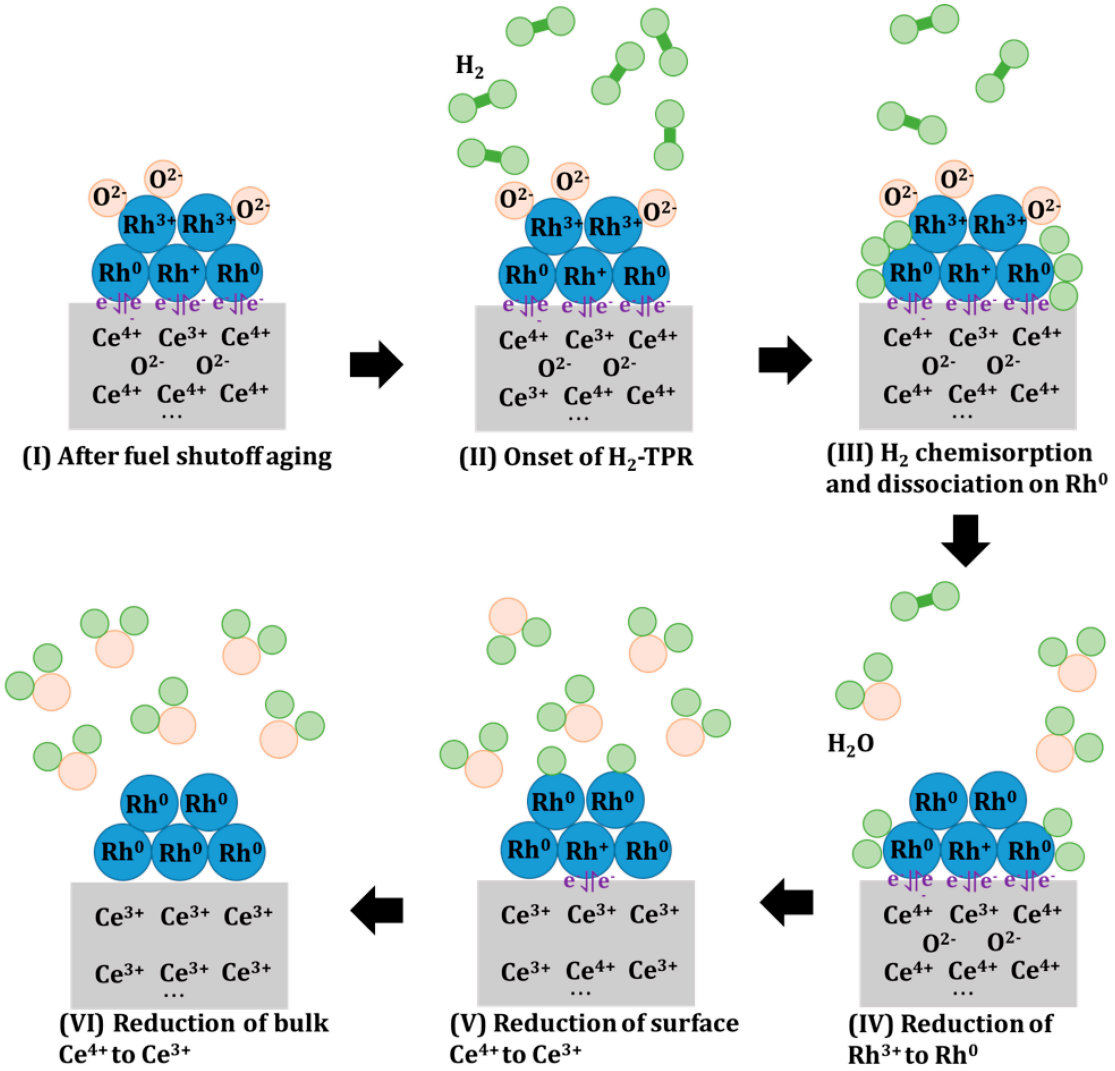

Figure 12. Speculative schematic of proposed redox reaction mechanism and interaction between $Rh^{\delta+}/Rh^0$ and Ce^{4+}/Ce^{3+} redox couple during H_2-TPR of 0.5% Rh/CZO. The redox reactions followed the order described below. (**I**) After simulated fuel shutoff aging in air at 800 °C, 950 °C, or 1050 °C, surface Rh sites are oxidized to Rh_2O_3, while the Rh sites in close contacts with Ce_xO_y remained in reduced states ($Rh^{\delta+}$, $0 < \delta < 1$), with $Rh^{\delta+}/Rh^0$ and Ce^{4+}/Ce^{3+} redox couple formed for enhancing electron transfer efficiency; (**II**) H_2 flow through the sample; (**III**) At low temperature regime around 100 °C to 120 °C, H_2 was chemisorbed and dissociated on the Rh^0 sites, followed by (**IV**) Reduction of Rh^{3+} to Rh^0; (**V**) Reduction of surface Ce^{4+} sites to Ce^{3+} promoted by the $Rh^{\delta+}/Rh^0$ and Ce^{4+}/Ce^{3+} redox couple; (**VI**) Reduction of bulk Ce^{4+} sites to Ce^{3+} when more H_2 molecules were chemisorbed and dissociated on Rh^0.

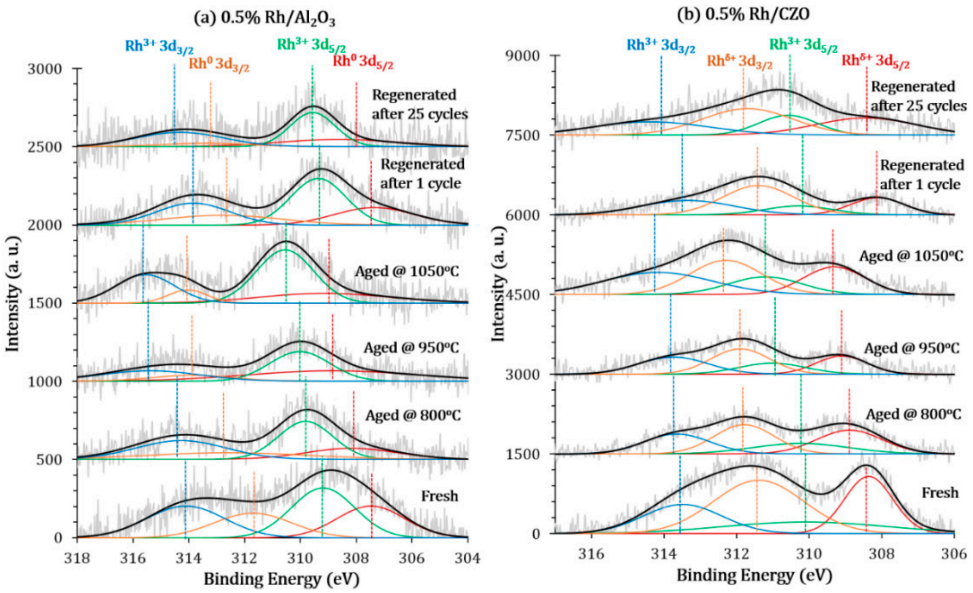

Figure 13. X-ray Photoelectron Spectroscopy (XPS) multiplex spectra in Rh 3d region (with BE of 318 eV–304 eV) of fresh, aged, and regenerated (**a**) 0.5% Rh/Al_2O_3 and (**b**) 0.5% Rh/CZO powder catalysts, and with aging temperature varied. Aged samples were achieved by aging the fresh catalysts in air at 800 °C, 950 °C or 1050 °C for 5 min. Regenerated samples were achieved by regenerating the aged ones (1050 °C for 5 min) using the method as described in Section 3.3.

Table 6. Summary of detailed information of XPS spectra as shown in Figure 12, *i.e.*, values of binding energy Rh $3d_{3/2}$ for Rh^{3+} and Rh^0 oxidation states, and Rh^{3+}/Rh^0 (or $Rh^{3+}/Rh^{\delta+}$) ratios [a] for fresh, aged, and regenerated 0.5% Rh/Al_2O_3 and 0.5% Rh/CZO samples.

Catalyst		*E* (Rh $3d_{3/2}$), eV		*E* (Rh $3d_{5/2}$), eV		Rh^{3+}/Rh^0 ($Rh^{3+}/Rh^{\delta+}$) [b]
		Rh^{3+}	Rh^0	Rh^{3+}	Rh^0	
0.5% Rh/Al_2O_3	Fresh	314.10	311.69	309.18	307.46	1.29
	800 °C aged for 5 min	314.27	312.59	309.81	308.16	1.51
	950 °C aged for 5 min	315.39	313.87	310.02	308.85	2.14
	1050 °C aged for 5 min	315.55	314.03	310.55	309.13	3.21
	Regenerated (I) [c]	313.83	312.78	309.35	307.34	1.41
	Regenerated (II) [d]	314.87	313.12	309.55	308.89	2.18
0.5% Rh/CZO	Fresh	313.49	311.39	310.10	308.36	0.48
	800 °C aged for 5 min	313.64	311.79	310.23	308.89	0.75
	950 °C aged for 5 min	313.74	311.90	311.02	309.10	0.81
	1050 °C aged for 5 min	314.17	312.30	311.21	309.31	0.99
	Regenerated (I) [c]	313.35	311.40	310.29	308.11	0.64
	Regenerated (II) [d]	314.01	311.70	310.70	308.44	0.70

[a] Rh^{3+}/Rh^0 ratio was calculated by comparing the integrated area under the corresponding fitted curves of Rh^{3+} $3d_{3/2}$ and Rh^0 $3d_{3/2}$ in Figure 6; [b] In Rh/Al_2O_3, Rh^{3+} and Rh^0 coexist, and Rh^{3+}/Rh^0 ratios are compared. In Rh/CZO, Rh^{3+} and $Rh^{\delta+}$ ($0 \leq \delta < 1$) coexist, and the $Rh^{3+}/Rh^{\delta+}$ ratios are compared; [c] Regenerated samples (I) were achieved by performing *in situ* regeneration using propane steam reforming with aged samples after aging at 1050 °C for 5 min; [d] Regenerated samples (II) were achieved after 25 cycles in the simulated fuel shutoff-regeneration cycle tests.

Fresh 0.5% Rh/Al_2O_3 displayed (1) an intense Rh^{3+} $3d_{5/2}$ peak at 309.2 eV; (2) a small Rh^0 $3d_{5/2}$ side peak at 307.5 eV; and (3) Rh^{3+}/Rh^0 ratio of 1.29. Consistent with the TPR result, the XPS data suggests the Rh sites in the fresh samples were partially oxidized. With increasing aging temperature, Rh 3d peaks shift to higher binding energy, together with increases in Rh^{3+}/Rh^0 ratio (1.29 → 1.51 → 2.14 → 3.21), suggesting a transition to a higher Rh oxidation state, *i.e.*, $Rh^0 \rightarrow Rh^{3+}$. It is known that the oxidation process increases Rh oxidation states while the reduction process has an opposite effect [48]. The non-reducible Rh phase was reported resulting from a diffusion of Rh^{3+} ions in subsurface regions of the alumina matrix. The binding energy of the new Rh phase is greater than that in Rh_2O_3, indicating a different state from that of Rh^{3+} in Rh_2O_3, which is ascribed to metal-support interaction [81].

Different from 0.5% Rh/Al_2O_3, low Rh valence state ($Rh^{\delta+}$, $0 < \delta < 1$) dominates in fresh 0.5% Rh/CZO ($Rh^{3+}/Rh^{\delta+}$ ratio of 0.48). For 0.5% Rh/CZO, Rh^0 $3d_{5/2}$ peaks display higher BE values. The small but definite electropositive shifts detected for Rh^0 peaks are ascribed to the existence of both Rh^0 and $Rh^{\delta+}$ species, giving evidence to the existence of $Rh^{\delta+}/Rh^0$ and Ce^{4+}/Ce^{3+} redox couple [63]. This assignment is in agreement with previous FT-IR result [82,83], which shows the existence of surface electron deficient $Rh^{\delta+}$ species present on CZO support. Like Rh/Al_2O_3, the $Rh^{3+}/Rh^{\delta+}$ ratio in Rh/CZO increased with aging temperature. It is also important to note that the way Rh3d peak is interpreted largely affects the result. The XPS Rh 3d spectra for Rh/CeO_2 system studied by Force *et al.* [84] was deconvoluted into three peaks, respectively assigned to Rh^0 (306.8 eV), Rh^+ (307.8 eV), Rh^{3+} (309.2 eV) states. While other systems have different interpretations [85]. In our Rh/CZO system, assigning XPS peaks to Rh^0 and $Rh^{\delta+}$ species is easier for comparison.

Furthermore, the reduced areas under Rh 3d peaks for aged samples suggests Rh sintering and/or Rh dissolution into sintered support during simulated fuel shutoff aging. The characterization result is in agreement with the findings by Kang *et al.* [20]. In their study, the effect of aging atmosphere on the sintering behavior of commercial Pd- or Rh-TWC as well as the TWC performance were investigated under straight oxidizing, reducing, and periodic cycling aging conditions. For Rh-TWC, the diffusion of Rh_2O_3 into the support along with the agglomeration of the Rh metal were found the main causes of catalyst deactivation during high temperature oxidative aging.

XPS Rh 3d spectra of regenerated 0.5% Rh/Al_2O_3 and 0.5% Rh/CZO in both show that after the first *in situ* regeneration, the oxidation state of Rh was significantly lowered, exposing more active Rh^0 species to the reactant atmosphere. This explains the enhanced reforming activity resulting from H_2 reduction (regeneration).

In summary, different types of interactions between Rh and support materials exist in Rh/Al_2O_3 and Rh/CZO during fuel shutoff aging. It is well known that strong interaction between Rh and Al_2O_3 with the formation of Rhodium Aluminate occurs in oxidative aging of Rh/Al_2O_3 [2]. Compared to aged Rh/Al_2O_3, the metal-support interaction in aged Rh/CZO occurs to a much lesser extent. Haneda *et al.* [86] reported that high-temperature aging can alter the surface properties of Ce_xO_y-ZrO_2 to inhibit the formation of formate species poisoning the catalytic active Rh sites.

The superior regenerability of 0.5% Rh/CZO was believed mainly contributed by the co-existence of Ce^{4+}/Ce^{3+} and $Rh^0/Rh^{\delta+}$ redox couple [87–90]. Wang *et al.* [62], investigated the interaction between Rh and Ce_xO_y in Rh-Ce_xO_y/Al_2O_3 catalyst system, with enhanced electron transfer efficiency during catalytic CO_2 dry reforming of CH_4. Similar promotional effect likely occurred with 0.5% Rh/CZO

catalyst during regeneration, as confirmed by TPR and XPS results. The electron transfer pathways during catalyst regeneration are proposed in Figure 14.

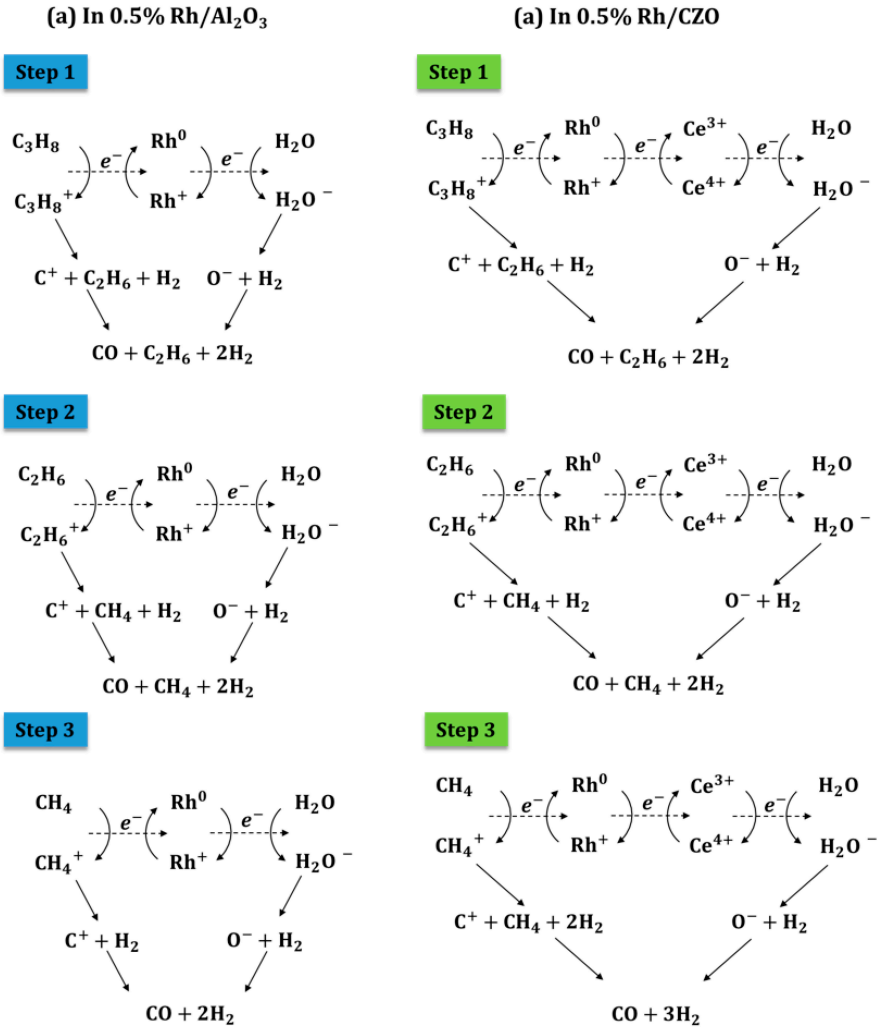

Figure 14. Proposed reaction mechanism and electron transfer pathways for steam reforming of propane on (**a**) Rh/Al_2O_3 and (**b**) Rh/CZO catalysts.

For Rh/Al_2O_3, electrons are first donated by hydrocarbons (reactant C_3H_8, and product C_2H_6 and CH_4), and then transferred through the redox circle of $Rh^0 \rightleftharpoons Rh^+$, and finally accepted by H_2O. Electron transfer is accompanied by redox reactions and the formation of H_2, CO, and intermediate products. For Rh/CZO, the coexistence of the Ce^{4+}/Ce^{3+} and the $Rh^0/Rh^{\delta+}$ redox couple allows availability of $Rh^{\delta+}$ species, to accept the electrons donated by HC more easily. The efficient electron transfer pathway results in the significant catalytic steam reforming performance of Rh/CZO.

3. Experimental Section

3.1. Catalyst Materials

The model catalysts studied were 0.5% Rh/Al_2O_3 and 0.5% Rh/Ce_xO_y-ZrO_2 (denoted as CZO with Ce:Zr atomic ratio of 1:2). The catalysts and reference support materials were supplied by BASF Iselin, NJ, USA. After impregnation of the precursor salts (proprietary) onto the support (γ-Al_2O_3 or CZO), a

25% solid slurry was created, ball milled, and calcined at 550 °C in N_2 to generate a catalyst powder sample with average particle size less than 30 μm, as estimated by SEM, Figure 15). The samples were stored in ambient air. XRD of 0.5% Rh/γ-Al_2O_3 showed a well-defined γ-Al_2O_3 support structure, with all the peaks indexed to a cubic unit cell (a = b = c = 7.900 Å, space group symmetry $Fd\bar{3}m$(227)) [91]. For 0.5% Rh/CZO, most of the support zirconia was observed incorporated into the ceria fluorite structure, with the formation of cubic symmetric $Ce_xZr_{(1-x)}O_2$ solid solution [92,93].

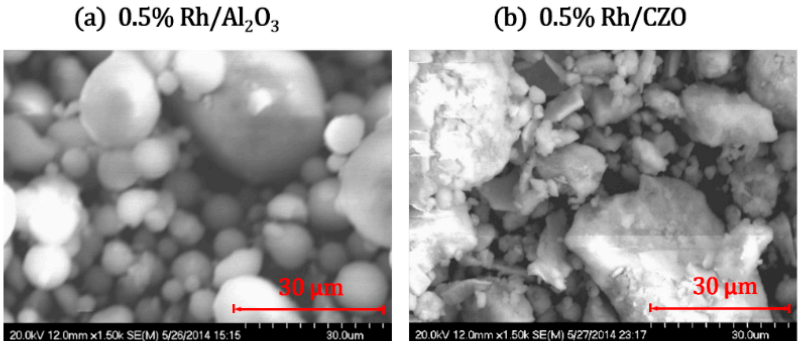

Figure 15. Scanning Electron Microscopic (SEM) images of fresh (**a**) 0.5% Rh/Al_2O_3 and (**b**) 0.5% Rh/CZO at μm scale. SEM measurement condition: beam voltage of 20 kV, beam current of 10 μm, working distance of 12 mm, and 30 μm in scale.

3.2. Simulated Fuel Shutoff Aging and Fuel Rich Regeneration Processes

Immediately prior to fuel shutoff aging, the TWC catalyst bed temperature is around 1000 °C generated under high load conditions. Upon fuel shutoff the introduction of air from the cylinder causes a short time increase in catalyst temperature by 15 °C to 20 °C due to the exothermic oxidation of adsorbed hydrocarbons on the catalyst surface. The catalyst bed temperature then begins to fall to about 800 °C in less than 10–15 s. During this high temperature-oxidizing environment the Rh reacts with the Al_2O_3 causing deactivation of the NO_x activity. Some of the US automobile companies use 1050 °C aging in air as a simulation of what is experimentally observed to insure stable catalyst performance for 150,000 miles of driving with periodic fuel shut off. We have adapted this procedure in our paper consistent with current practice. For more details about the catalyst temperature profiles during fuel shutoff, please refer to a previous SAE Technical Paper [16].

The schematic reactor system is sketched in Figure 16. During aging, 0.0702 mL (around 0.05 g) of powdered catalyst, well mixed with 0.25 mL quartz sand as a diluent, was loaded into a quartz tube reactor (ID of 10.5 mm, OD of 12.7 mm) with a quartz frit fused in the middle to hold the sample in place. The reactor was housed in an infrared furnace. Air flowed into the reactor system at 3400 mL/h through a calibrated gas flow controller (MKS 647 C, MKS Instrument Inc., Andover, MA, USA) with multiple gas channels. Reaction temperature of the catalyst bed was monitored by a thermocouple (Omega K type) placed at the inlet to the catalyst.

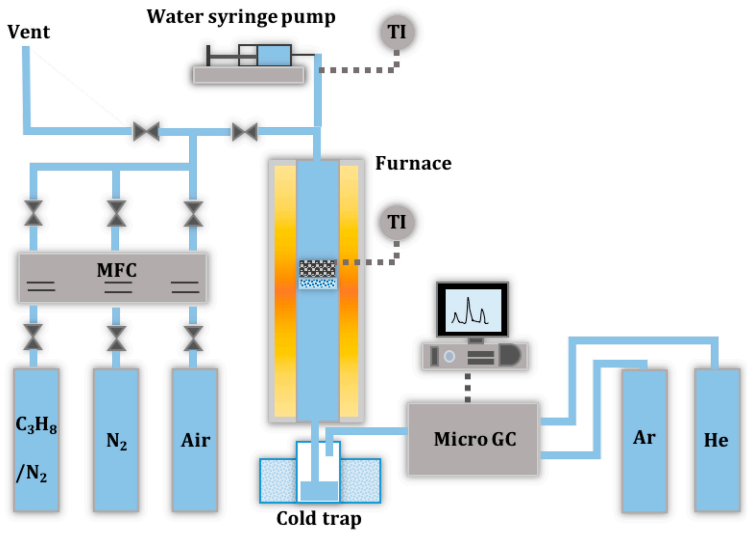

Figure 16. Schematic of the packed bed flow reactor and analysis system. (MFC: Mass Flow Controller, GC: Gas Chromatography, TI: Temperature Indicator).

Catalyst regeneration was performed *in situ* by exposing the aged catalyst to reducing conditions. During regeneration the Rh catalyzes steam reforming (SR), generating H_2, which reduces Rh^{3+} to its active metallic state Rh^0.

The regeneration feed gas mixture of 500 vppm propane, 10 vol-% steam, 8 vol-% CO_2, and N_2 in balance, with a total GHSV of 120,000 h^{-1} was used to simulate the engine exhaust at slightly fuel rich conditions. Propane is commonly used as a model compound [30,31,94,95] for the HC species. Liquid water was injected at 0.68 mL/h by a syringe pump (Cole Parmer), vaporized at around 120 °C, and mixed with the incoming gas feed. The regeneration temperature was maintained 550 °C for 1 h with H_2 production continuously monitored. Temperatures of the water evaporator T_W and catalyst bed T_{bed} were monitored by thermocouples. A cold trap was placed downstream to condense the unreacted water, and a calibrated micro GC (Inficon 3000, INFICON Inc., New York, NY, USA, equipped with 10 m Molsieve 5A column, 8 m Plot U column, and thermal conductivity detectors) was used for online analysis of the gas products every three minutes. The regenerated sample was then cooled in air to room temperature, and preserved in ambient air.

3.3. Catalyst Regenerability as Measured at Simulated Fuel Rich Condition

Activity tests were performed with the same reaction feed as that in regeneration, but with temperature scans from 200 °C to 550 °C, with 50 °C increments, and a 30 min-hold at each temperature. The catalytic conversions were conducted far from equilibrium.

3.4. Catalyst Stability during Simulated Fuel Shutoff Aging-Fuel Rich Regeneration Cycle Tests

Fuel shutoff aging-fuel rich regeneration cycle tests (25 cycles in total) were performed to simulate the automotive engine operation cycles, as shown in Figure 17a,b respectively. Simulated fuel shutoff and regeneration conditions were maintained as described in Section 3.2, except the aging temperature of 1050 °C was used. Activity of the regenerated catalysts after every five cycles were measured, as described in Section 3.3.

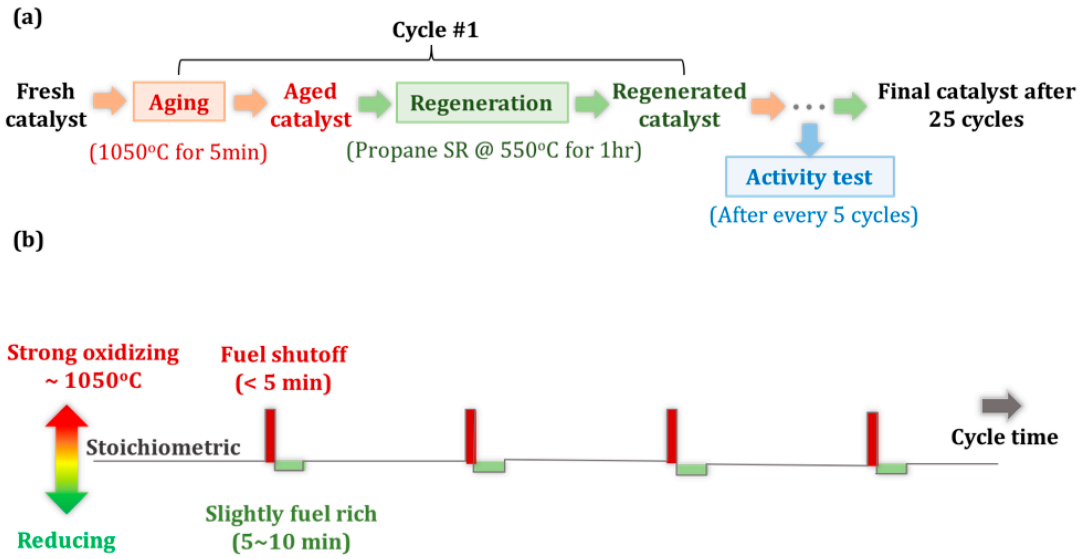

Figure 17. Schematic process flow diagrams of (**a**) simulated fuel shutoff aging-fuel rich regeneration cycle and activity test; and (**b**) on-board gasoline engine fuel shutoff-fuel rich operation cycles.

3.5. Data Analysis for Catalyst Activity Tests

During catalyst activity tests, the mole flow rate Q_i (mol/h) of each gas product component (H_2, N_2, CO, CH_4, CO_2, C_3H_8, except for water, which was condensed before GC analysis) was determined by Equation (1).

$$Q_{\mathrm{i}} = Q_{\mathrm{N_2}} \times \frac{F_{\mathrm{i}}}{F_{\mathrm{N_2}}} \quad (1)$$

where $Q_{\mathrm{N_2}}$ is the mole flow rate of the carrier gas N_2 (also the internal standard, 0.3383 mol/h). F_i is the mole percentage of compound i in the gas product mixture as analyzed by the online micro GC. Thermodynamic modeling at the same reaction condition was performed by HSC Chemistry 5.

3.6. Catalyst Characterization

SEM images were taken with a Hitachi S-4700 I Cold Field Emission Scanning Electron Microscope (Hitachi High Technologies America Inc., Schaumburg, IL, USA. Accelerating voltage of 20 kV, emission current of 10 μA, and working distance of 12 mm were used. Multiple pictures at different spots within the same measured sample were collected in each measurement.

XRD patterns of catalyst samples were generated with a Scintag XDS-2000 unit (Scintag Inc., Cupertino, CA, USA). The powdered samples were scanned between 15° and 80° with an incremental step of 0.02° and preset time of 2 s.

The Brunauer-Emmett-Teller (BET) surface areas of catalysts were determined using a Quantachrome ChemBET Pulsar TPR/TPD unit (Quantachrome Instrument, Boynton Beach, FL, USA), equipped with a TCD detector. About 0.05 g of catalyst sample was outgassed in pure N_2 at 200 °C for 2 h, while subsequent N_2 adsorption was performed using 30% N_2/He at liquid N_2 temperature (−195.6 °C). The

TCD signal was calibrated using an external standard method, and monolayer N_2 adsorption was evaluated by single point BET method.

The metal dispersions of catalysts were measured by CO- selective chemisorption using the same Quantachrome unit. About 0.1 g of catalyst sample was heated in pure He at 200 °C for 120 min, followed by pre-reduction in 10% H_2/Ar at 400 °C for 120 min. CO (99.9% purity) adsorption, with automatic injection volume of 285 μL per pulse, was performed at 40 °C after pre-reduction. CO chemisorption capacity of each catalyst sample was evaluated based on the total volume of adsorbed CO at standard condition ($V_{CO,std}$, L). Metal dispersion (D_M) is calculated according to Equation (2):

$$\text{Dispersion } (\%) = \frac{1}{n} \times \frac{V_{\text{CO},std}}{22.4} \times \frac{M_M}{m_s \times y_M} \times 100\% \quad (2)$$

where M_M is the metal atomic weight (102.9 g/mol for Rh). The catalyst weight and metal content are designed by m_s and y_M respectively. The CO-to-metal site stoichiometry n was assumed to be 2 in accordance with current literature [20,96].

The Transmission Electron Microscopic (TEM) observations of the fresh, aged, and regenerated samples were taken with a JEOL 100CX-II TEM unit (JOEL Inc., Peabody, MA, USA). The TEM measurements were operated at an accelerating voltage of 100 kV. The catalyst powder sample was dispersed in pure ethanol (200 proof), followed by sonication for 3 h, and deposition on a Lacey carbon film supported Cu grid (200 mesh). For each sample, 50~60 TEM images with different magnifications at multiple spots were taken, and no less than 400 individual palladium particles were counted with ImageJ software. The mean surface area-weighted palladium particle size is calculated using Equation (3):

$$d_{TEM} = \frac{\sum_i n_i d_i^3}{\sum_i n_i d_i^2} \quad (3)$$

where n_i is the number of particles in ferret diameter d_i and $\sum_i n_i > 400$.

The redox properties of catalysts were studied by TPR. The measurements were carried out with the same Quantachrome unit as above. About 0.1 g of catalyst sample was first outgassed in pure Helium at 150 °C for 2 h, and cooled to room temperature. TPR analysis was performed subsequently by heating a sample located in a U-tube reactor to 800 °C at 5 °C/min, with 4% H_2/N_2 flowing through the sample. The TCD signal (corresponding to H_2 uptake) was then normalized to per gram of catalyst.

Ex situ XPS spectra of catalysts were measured with a Perkin-Elmer PHI 5500 XPS instrument (Physical Electronics Inc., Chanhassen, MN, USA) equipped with a Mg Kα monochromatic source. The samples were prepared by fixing catalyst powder onto a double-sided carbon sticky tape. The XPS main chamber was evacuated to 10^{-9} Torr. C 1s peak with standard binding energy of 284.6 eV was used for peak position calibration. AugerScan and Origin software were used for spectra data analysis. NIST XPS online database and other literature sources were used for peak assignments.

4. Conclusions

Automotive three way catalysts (TWC) experience severe deactivation during fuel shutoff when exposed to an oxidizing environment at temperatures up to 1050 °C. A return of air-to-fuel ratio to slight rich ($\lambda < 1$) allows *in situ* catalyst regeneration by H_2 generated mainly through catalytic

steam reforming. The paper examined the effects of oxidative fuel shutoff and simulated fuel rich regeneration on the activity and chemistry of the Rh component in TWC. 0.5% Rh/Al_2O_3 and 0.5% Rh/CZO are compared.

For both supported Rh catalysts, deactivation is accelerated with increasing oxidative aging temperature. Metal and support sintering, reversible metal oxidation, and metal-support interactions were found in both catalysts but to widely different extents. Compared to the strong metal-support interactions (with the formation of rhodium aluminate) in Rh/Al_2O_3, the interactions in Rh/CZO during simulated fuel shutoff was weaker and more readily reversible.

Partial catalyst regeneration is accomplished by reducing Rh to its active metallic state (Rh^0) thereby "releasing" it from the metal-support interactions. Stable catalytic performance is achieved by periodic aging-regeneration cycle tests (25 cycles in total). Compared to Rh/Al_2O_3, Rh/CZO showed more rapid response to regeneration and maintained higher stability. The existence of $Rh^{\delta+}/Rh^0$ and Ce^{3+}/Ce^{4+} redox pair in Rh/CZO was confirmed by TPR and XPS, which was believed promoting the catalyst regenerability by enhancing the electron transfer efficiency during catalytic steam reforming.

This study is consistent with the known practice, used in gasoline vehicles, of fuel shutoff followed by a slightly rich mode to regenerate the Rh component and the NO_x activity.

Acknowledgments

Financial support by BASF is greatly acknowledged. Meanwhile, the authors are grateful to the Shared Materials Characterization Lab at Columbia University for XPS and XRD instruments. The authors would also like to thank the lab assistances by Kyle Misquitta, Yi Li, and Anh Nguyen.

Author Contributions

The present work was conducted under the supervision of Robert Farrauto, with Qinghe Zheng, Michel Deeba, and Ioannis Valsamakis as authors at Columbia University and BASF in 2014~2015. Robert Farrauto did the main research consulting and paper editing, and is named the correspondent author of the submitted work. Qinghe Zheng did the main experimental work (reactor tests and catalyst characterizations) and paper writing, and is named the primary author. Michel Deeba synthesized the catalyst materials and has been the project senior consultant. Ioannis Valsamakis set up the reactor and explored some of the reaction conditions.

Conflicts of Interest

The authors declare no conflict of interest.

References

1. Bartholomew, C.H.; Farrauto, R.J. *Fundamentals of Industrial Catalytic Process*, 2nd ed.; John Wiley & Sons: Iselin, NJ, USA, 2005; pp. 713–724.
2. Heck, R.M.; Farrauto, R.J.; Gulati, S. *Catalytic Air Pollution Control: Commercial Technology*, 3rd ed.; John Wiley & Sons: Iselin, NJ, USA, 2009; pp. 103–176.

3. Farrauto, R.J.; Heck, R.M. Catalytic converters: State of the art and perspectives. *Catal. Today* **1999**, *51*, 351–360.
4. Yamada, T.; Kayano, K.; Funabiki, M. The effectiveness of Pd for converting hydrocarbons in TWC catalysts. *SAE Tech. Pap.* **1993**, doi:10.4271/930253.
5. Liu, Y.; Dettling, J. Evolution of Pd/Rh TWC catalyst technology. *SAE Tech. Pap.* **1993**, doi:10.4271/930249.
6. Kaspar, J.; Fornasiero, P.; Hickey, N. Automotive catalytic converters: Current status and some perspectives. *Catal. Today* **2003**, *77*, 419–449.
7. Deganello, F.; Martorana, A. Phase analysis and oxygen storage capacity of Ceria-Lathana-based TWC promoters prepared by Sol-Gel routes. *J. Solid State Chem.* **2002**, *163*, 527–533.
8. Martorana, A.; Deganello, G.; Longo, A.; Prestianni, A.; Liotta, L.; Macaluso, A.; Pantaleo, G.; Balerna, A.; Mobilio, S. Structural evolution of Pt/ceria-zirconia TWC catalysts during the oxidation of carbon monoxide. *J. Solid State Chem.* **2004**, *177*, 1268–1275.
9. Hirasawa, Y.; Katoh, K.; Yamanda, T.; Kohara, A. Study on new characteristic CeO_2-ZrO_2 based material for advanced TWC. *SAE Tech. Pap.* **2009**, doi:10.4271/2009-01-1078.
10. Farrauto, R.J.; Heck, R.M. Environmental catalysis into the 21st century. *Catal. Today* **2000**, *55*, 179–187.
11. Dettling, J.C. High Performance Thermally Stable Catalyst. U.S. Patent 5,212,142, 18 May 1993.
12. Yamada, T.; Kobayashi, T.; Kayano, K.; Funabiki, M. Development of Zr containing TWC catalysts. *SAE Tech. Pap.* **1997**, doi:10.4271/970466.
13. Farra, R.; Garcia-Melchor, M.; Eichelbaum, M.; Hashagen, M.; Frandsen, W.; Allan, J.; Girgsdies, F.; Szentmiklosi, L.; Lopez, N.; Teschner, D. Promoted Ceria: A structural, catalytic, and computational study. *ACS Catal*. **2014**, 3, 2256-2268.
14. Brehob, D.D.; Kappauf, T.A.; Anderson, R.W. Direct Injection Spark Ignition Engine having Deceleration Fuel Shutoff. U.S. Patent 5,941,211 A, 24 August 1999.
15. Bidner, D.; Lopez, R.; Doering, J.; Manning, S. System and Method to Improve Drivability with Deceleration Fuel Shutoff. U.S. Patent 7,591,758 B2, 22 September 2009.
16. Brinkmeier, C.; Schön, C.; Vent, G.; Enderle, C. Catalyst temperature rise rise during deceleration with fuel cut. *SAE Tech. Pap.* **2006**, doi:10.4271/2006-01-0411.
17. Heck, R.M.; Farrauto, R.J. Automotive exhaust catalysts. *Appl. Catal. A* **2001**, *221*, 443–457.
18. Force, C.; Paniego, A.R.; Guil, J.M.; Gatica, J.M.; Lopez-Cartes, C.; Bernal, S.; Sanz, J. Metal sintering in Rh/Al_2O_3 catalysts followed by HREM, ^1H NMR, and H_2 chemisorption. *Langmuir* **2001**, *17*, 2720–2726.
19. Bernal, S.; Calvino, J.J.; Cauqui, M.A.; Perez Omil, J.A.; Pintado, J.M.; Rodriguez-Izquierdo, J.M. Image simulation and experimental HREM study of the metal dispersion in Rh/CeO_2 catalysts. Influence of the reduction/reoxidation conditions. *Appl. Catal. B* **1998**, *16*, 127–138.
20. Kang, S.B.; Han, S.J.; Nam, S.B.; Nam, I.; Cho, B.K.; Kim, C.H.; Oh, S.H. Effect of aging atmosphere on thermal sintering of modern commercial TWCs. *Top. Catal.* **2013**, *56*, 298–305.
21. Gandhi, H.S.; Graham, G.W.; McCabe, R.W. Automotive exhaust catalysis. *J. Catal.* **2003**, *216*, 433–442.

22. Salazar-Villalpando, M.D.; Berry, D.A.; Gardner, T.H. Partial oxidation of methane over Rh/supported-ceria catalysts: Effect of catalyst reducibility and redox cycles. *Int. J. Hydrogen Energy* **2008**, *33*, 2695–2703.
23. Vedyagin, A.A.; Volodin, A.M.; Stoyanovskii, V.O.; Kenzhin, R.M.; Slavinskaya, E.M.; Mishakov, I.V.; Plyusnin, P.E.; Shubin, Y.V. Stabilization of active sites in alloyed Pd-Rh catalysts on γ-Al_2O_3 support. *Catal. Today* **2014**, *238*, 80–86.
24. Imamura, S.; Yamashita, T.; Hamada, R.; Saito, Y.; Nakao, Y.; Tsuda, N.; Kaito, C. Strong interaction between rhodium and ceria. *J. Mol. Catal.* **1998**, *129*, 249–256.
25. Bernal, S.; Botana, F.J.; Calvino, J.J.; Cauqui, M.A.; Cifredo, G.A.; Jobacho, A.; Pintado, J.M.; Rodríguez-Izquierdo, J.M. Microstructural and chemical properties of ceria-supported rhodium catalysts reduced at 773 K. *J. Phys. Chem.* **1993**, *97*, 4118–4123.
26. Soria, J.; Martinez-Arias, A.; Conesa, J.C. Effect of oxidized rhodium on oxygen adsorption on cerium oxide. *Vacuum* **1992**, *43*, 437–440.
27. Bernal, S.; Botana, F.J.; Calvino, J.J.; Cifredo, G.A.; Perez-Omil, J.A.; Pintado, J.M. HREM study of the behavior of a Rh/CeO_2 catalyst under high temperature reducing and oxidizing conditions. *Catal. Today* **1995**, *23*, 219–250.
28. Bernal, S.; Blanco, G.; Calvino, J.J.; Cifredo, G.A.; Omil, J.A.P.; Pintado, J.M.; Yaro, A. HRTEM and TPO study of the behavior under oxidizing conditions of some Rh/CeO_2 catalysts. *Stud. Surf. Sci. Catal.* **1994**, *82*, 507–514.
29. Trovarelli, A. Catalytic properties of ceria and CeO_2-containing materials. *Catal. Rev. Sci. Eng.* **1996**, *38*, 439–520.
30. Padeste, C.; Cant, N.W.; Trimm, D.L. Reactions of ceria supported rhodium with hydrogen and nitric oxide studied with TPR/TPO and XPS techniques. *Catal. Lett.* **1994**, *28*, 301–331.
31. Williamson, W.B.; Lewis, D.; Perry, J.; Gandhi, H.S. Durability of palladium automotive catalysts: Effects of trace lead levels, exhaust composition, and misfueling. *Ind. Eng. Chem. Prod. Res. Dev.* **1984**, *23*, 531–536.
32. Otto, K.; Sulak, R.J. Effects of manganese deposits from MMT on automotive catalysts in the absence and presence of other fuel additives. *Environ. Sci. Technol.* **1978**, *12*, 181–184.
33. Sayle, T.X.T.; Parker, S.C.; Catlow, C.R.A. Surface segregation of metal ions in cerium dioxide. *J. Phys. Chem.* **1994**, *98*, 13625–13630.
34. Sanchez, M.G.; Gazquez, J.L. Oxygen vacancy model in strong metal-support interaction. *J. Catal.* **1987**, *104*, 120–135.
35. Heo, I.; Yoon, D.Y.; Cho, B.K.; Nam, I.; Choung, J.W.; Yoo, S. Activity and thermal stability of Rh-based catalytic system for an advanced modern TWC. *Appl. Catal. B* **2012**, *121–122*, 75–87.
36. Hochmuth, J.K. Engine Management Strategy to Improve the Ability of a Catalyst to Withstand Severe Operating Environments. U.S. Patent 6,021,638, 2 February 2000.
37. Theis, J.R.; Kerns, J.M.; Uhrich, M.J.; Cavataio, G.; Leone, T.G.; Doering, J.A.; Rumpsa, T.A. NO_x Control during Engine Idle-Stop Operation. U.S. Patent 0,039,781 A1, 6 Februray 2014.
38. Gonzalez-Valasco, J.R.; Botas, J.A.; Ferret, R.; Gonzalez-Marcos, M.P.; Marc, J.L.; Gutierrez-Ortiz, M.A. Thermal aging of Pd/Pt/Rh automotive catalysts under a cycled oxidizing-reducing environment. *Catal. Today* **2000**, *59*, 395–402.

39. Campbell, B.; Farrington, R.; Inman, G.; Dinsdale, S. Improved Three Way Catalyst Performance Using an Active Bias Control Regeneration System. *SAE Tech. Pap.* **2000**, doi:10.4271/2000-01-0499.
40. Leone, T.G.; Ulrey, J.N.; Dearth, M.A. Engine Control for Catalyst Regeneration. U.S. Patent 9,016,244 B2, 28 April 2015.
41. Santillo, M.; Jankovic, M.J.; Magner, S.W.; Uhrich, M.J. Two-Stage Catalyst Regeneration. U.S. Patent 0,051,812 A1, 19 February 2015.
42. Doering, J.; Bidner, D.; Elwart, S. System and Method to Reduce Stall during Deceleration Fuel Shutoff. U.S. Patent 7,998,027 B2, 16 August 2011.
43. Shelef, M.; Graham, G.W. Why rhodium in automotive three-way catalysts. *Catal. Rev. Sci. Eng.* **1994**, *36*, 433–457.
44. Morikawa, A.; Tanabe, T.; Hatanaka, M.; Takahashi, N.; Sato, A.; Kuno, O.; Suzuki, H.; Shinjoh, H. Inhibition of Rh sintering and improved reducibility of Rh on ZrO_2 nanocomposite with an Al_2O_3 diffusion barrier. *Appl. Catal. A* **2015**, *493*, 33–39.
45. Tauster, S. Base metal oxide promoters in TWC catalysts. *SAE Tech. Pap.* **1993**, doi:10.4271/930250.
46. Kolb, G.; Zapf, R.; Hessel, V.; Lowe, H. Propane steam reforming in micro-channels-results from catalyst screening and optimisation. *Appl. Catal. A* **2004**, *277*, 155–166.
47. Zheng, Q.; Janke, C.; Farrauto, R. Steam reforming of sulfur-containing dodecane on a Rh-Pt catalyst: Influence of process parameters on catalyst stability and coke structure. *Appl. Catal. B* **2014**, *160–161*, 525–533.
48. Barin, I. *Thermochemical Data of Pure Substances*; VCH: New York, NY, USA, 1989.
49. Heck, R.; Hochmuth, J.; Detting, J. Effect of oxygen concentration on aging of TWC catalysts. *SAE Tech. Pap.* **1992**, doi:10.4271/920098.
50. Hwang, C.; Yeh, C.; Zhu, Q. Rhodium-oxide species formed on progressive oxidation of rhodium clusters dispersed on alumina. *Catal. Today* **1999**, *51*, 93–101.
51. Soria, J.; Martinez-Arias, A.; Coronado, J.M.; Conesa, J.C. Influence of the support on the metal dispersion in Rh/CeO_2 catalysts. *Appl. Surf. Sci.* **1993**, *70–71*, 245–249.
52. Duarte, R.B.; Krumeich, F.; van Bokhoven, J.A. Structure, activity, and stability of atomically dispersed Rh in methane steam reforming. *ACS Catal*. **2014**, *4*, 1279–1286.
53. Barbier, J., Jr.; Duprez, D. Reactivity of steam in exhaust gas catalysis. Part II: Sintering and regeneration of Rh and PtRh catalysts in propane oxidation. *Stud. Surf. Sci. Catal.* **1995**, *96*, 73–84.
54. Fallah, J.E.; Boujana, S.; Dexpert, H.; Kiennemann, A.; Majerus, J.; Touret, O.; Villain, F.; Normand, F.L. Redox processes on pure ceria and on Rh/CeO_2 catalyst monitored by X-ray absorption (fast acquisition mode). *J. Phys. Chem.* **1994**, *98*, 5522–5533.
55. Trovarell, A.; Dolcetti, G.; Leitenburg, C.; Kaspar, J.; Finetti, P.; Santoni, A. $Rh\text{-}CeO_2$ interaction induced by high-temperature reduction. Characterization and catalytic behavior in transient and continuous conditions. *J. Chem. Soc. Faraday Trans.* **1992**, *88*, 1311–1319.
56. Benseradj, F.; Sadi, F.; Chater, M. Hydrogen spillover studies on diluted Rh/Al_2O_3 catalyst. *Appl. Catal. A* **2002**, *228*, 135–144.

57. Hori, C.E.; Permana, H.; Ng, K.Y.S.; Brenner, A.; More, K.; Rahmoeller, K.M.; Belton, D. Thermal stability of oxygen storage properties in a mixed CeO_2-ZrO_2 system. *Appl. Catal. B* **1998**, *16*, 105–117.
58. Monte, R.D.; Kaspar, J. On the role of oxygen storage in three-way catalysis. *Top. Catal.* **2004**, *28*, 47–57.
59. Boaro, M.; Vicario, M.; Leitenburg, C.; Dolcetti, G.; Trovarelli, A. The use of temperature-programmed and dynamic/transient methods in catalysis: Characterization of ceria-based, model three-way catalysts. *Catal. Today* **2003**, *77*, 407–417.
60. Miyazawa, T.; Okumura, K.; Kunimori, K.; Tomishige, K. Promotion of oxidation and reduction of Rh species by interaction of Rh and CeO_2 over Rh/CeO_2/SiO_2. *J. Phys. Chem. C* **2008**, *112*, 2574–2583.
61. Duarte, R.B.; Safonova, O.V.; Krumeich, F.; Makosch, M.; van Bokhoven, J.A. Oxidation state of Ce in CeO_2 promoted Rh/Al_2O_3 catalysts during methane steam reforming: H_2O activation and alumina stablization. *ACS Catal.* **2013**, *3*, 1956–1964.
62. Wang, R.; Xu, H.; Liu, X.; Ge, Q.; Li, W. Role of redox couples of $Rh^0/Rh^{\delta+}$ and Ce^{4+}/Ce^{3+} in CH_4/CO_2 reforming over Rh-CeO_2/Al_2O_3 catalyst. *Appl. Catal. A* **2006**, *305*, 204–210.
63. Wu, X.; Xu, L.; Weng, D. The thermal stability and catalytic performance of Ce-Zr promoted Rh-Pd/γ-Al_2O_3 automotive catalysts. *Appl. Surf. Sci.* **2004**, *221*, 375–383.
64. Muraki, H.; Zhang, G. Design of advanced automotive exhaust catalysts. *Catal. Today* **2000**, *63*, 337–345.
65. Fornasiero, P.; Monte, R.D.; Rao, G.R.; Kaspar, J.; Meriani, S.; Trovarelli, A.; Graziani, M. Rh-loaded CeO_2-ZrO_2 solid-solutions as highly efficient oxygen exchangers: Dependence of the reduction behavior and the oxygen storage capacity on the structural properties. *J. Catal.* **1995**, *151*, 168–177.
66. Nunan, J.; Williamson, W.; Robota, H. Advanced TWC technologies using CeO_2/ZrO_2 solid solutions. *SAE Tech. Pap.* **1996**, doi:10.4271/960798.
67. Cuif, J.; Blanchard, G.; Touret, O.; Seigneurin, A.; Marczi, M.; Quemere, E. (Ce, Zr)O_2 solid solutions for three-way catalysts. *SAE Tech. Pap.* **1997**, doi:10.4271/970463.
68. Vlaic, G.; Fornasiero, P.; Geremia, S.; Kaspar, J.; Graziani, M. Relationship between the zirconia-promoted reduction in the Rh-loaded $Ce_{0.5}Zr_{0.5}O_2$ mixed oxide and the Zr–O local structure. *J. Catal.* **1997**, *168*, 386–392.
69. Diagne, C.; Idriss, H.; Kiennemann, A. Hydrogen production by ethanol reforming over Rh/CeO_2-ZrO_2 catalysts. *Catal. Commun.* **2002**, *3*, 565–571.
70. Salasc, S.; Perrichon, V.; Primet, M.; Mouaddib-Moral, N. Titration by oxygen of the spill-over hydrogen adsorbed on ceria-zirconia supported palladium-rhodium catalysts. *J. Catal.* **2002**, *206*, 82–90.
71. Rohart, E.; Verdier, S.; Demourgues, A.; Harle, V.; Pacaud, B.; Baylet, A.; Takemori, H.; Suda, E.; Allain, M. New CeO_2-ZrO_2 mixed oxides with improved redox properties for advanced TWC catalysts. *SAE Tech. Pap.* **2006**, doi:10.4271/2006-01-0852.
72. Lambrou, P.S.; Costa, C.N.; Christou, S.Y.; Efstathiou, A.M. Dynamics of oxygen storage and release on commercial aged Pd-Rh three-way catalysts and their characterization by transient experiments. *Appl. Catal. B* **2004**, *54*, 237–250.

73. Larichev, Y.V.; Netskina, O.V.; Komova, O.V.; Simagina, V.I. Comparative XPS study of Rh/Al_2O_3 and Rh/TiO_2 as catalysts for $NaBH_4$ hydrolysis. *Int. J. Hydrogen Energy* **2010**, *35*, 6501–6507.
74. Wang, Y.; Song, Z.; Ma, D.; Luo, H.; Liang, D.; Bao, X. Characterization of Rh-based catalysts with EPR, TPR, IR, and XPS. *J. Mol. Catal. A* **1999**, *149*, 51–61.
75. Zimowska, M.; Wagner, J.B.; Dziedzic, J.; Camra, J.; Borzecka-Prokop, B.; Najbar, M. Some aspects of metal-support strong interactions in Rh/Al_2O_3 catalyst under oxidizing and reducing conditions. *Chem. Phys. Lett.* **2006**, *417*, 137–142.
76. DeCaluwe, S.C.; Grass, M.E.; Zhang, C.; Gabaly, F.E.; Bluhm, H.; Liu, Z.; Jackson, G.S.; McDaniel, A.H.; McCarty, K.F.; Farrow, R.L.; *et al*. *In situ* characterization of ceria oxidation states in high-temperature electrochemical cells with ambient pressure XPS. *J. Phys. Chem. C* **2010**, *114*, 19853–19861.
77. Brun, M.; Berthet, A.; Bertolin, J.C. XPS, AES and Auger parameter of Pd and PdO. *J. Electron Microsc.* **1999**, *104*, 55–60.
78. He, Q.L.; Lai, Y.H.; Lu, Y.; Law, K.T.; Sou, L.K. Surface reactivity enhancement on a Pd/Bi_2Te_3 heterostructure through robust topological surface states. *Sci. Rep.* **2013**, *3*, doi:10.1038/srep02497.
79. Dohmae, K.; Nonaka, T.; Seno, Y. Local structure change of Rh on alumina after treatments in high-temperature oxidizing and reducing environments. *Surf. Interface Anal.* **2005**, *37*, 115–119.
80. Nagao, Y.; Nakahara, Y.; Sato, T.; Iwakura, H.; Takeshita, S.; Minami, S.; Yoshida, H.; Machida, M. Rh/ZrP_2O_7 as an efficient automotive catalyst for NO_x reduction under slightly lean conditions. *ACS Catal.* **2015**, *5*, 1986–1994.
81. Delahay, G.; Duprez, D. Effects of dispersion and partial reduction on the catalytic properties of Rh/Al_2O_3 catalysts in the steam reforming of mono-and bicyclic aromatics. *J. Catal.* **1989**, *115*, 542–550.
82. Haneda, M.; Shinoda, K.; Nagane, A.; Houshito, O.; Takagi, H.; Nakahara, Y.; Hiroe, K.; Fujitani, T.; Hamada, H. Catalytic performance of rhodium supported on ceria-zirconia mixed oxides for reduction of NO by propane. *J. Catal.* **2008**, *259*, 223–231.
83. Fontaine-Gautrelet, C.; Krafft, J.; Djega-Mariadassou, G.; Thomas, C. Evidence for Rh electron deficient atoms ($Rh^{\delta+}$) as the catalytic species for CO oxidation when supported on $Ce_{0.68}Zr_{0.32}O_2$. *J. Catal.* **2007**, *247*, 34–42.
84. Force, C.; Roman, E.; Guil, J.M.; Sanz, J. XPS and 1H NMR study of thermally stabilized Rh/CeO_2 catalysts submitted to reduction/oxidation treatments. *Langmuir* **2007**, *23*, 4569–4574.
85. Suopanki, A.; Polvinen, R.; Valden, M.; Harkonen, M. Rh oxide reducibility and catalytic activity of model Pt-Rh catalysts. *Catal. Today* **2015**, *100*, 327–330.
86. Haneda, M.; Houshito, O.; Sato, T.; Takagi, H.; Shinoda, K.; Nakahara, Y.; Hiroe, K.; Hamada, H. Improved activity of Rh/CeO_2-ZrO_2 three-way catalyst by high temperature ageing. *Catal. Commun.* **2010**, *11*, 317–321.
87. Parres-Esclapez, S.; Illan-Gomez, M.J.; Lecea, C.S.; Bueno-Lopez, A. On the importance of the catalyst redox properties in the N_2O decomposition over alumina and ceria supported Rh, Pd, and Pt. *Appl. Catal. B* **2010**, *96*, 370–378.
88. Bueno-Lopez, A.; Such-Basanez, I.; Lecca, C.S. Stabilization of active Rh_2O_3 species for catalytic decomposition of N_2O on La-, Pr- doped CeO_2. *J. Catal.* **2006**, *244*, 102–112.

89. He, H.; Dai, H.X.; Ng, L.H.; Wong, K.W.; Au, C.T. Pd-, Pt-, and Rh-doped $Ce_{0.6}Zr_{0.35}Y_{0.05}O_2$ three way catalysts: An investigation on performance and redox properties. *J. Catal.* **2002**, *206*, 1–13.
90. Hickey, N.; Fornasiero, P.; Kaspar, J.; Gatica, J.M.; Bernal, S. Effects of the nature of the reducing agent on the transient redox behavior of $NM/Ce_{0.68}Zr_{0.32}O_2$ (NM = Pt, Pd, and Rh). *J. Catal.* **2001**, *200*, 181–193.
91. Liu, Y.; Ma, D.; Han, X.; Bao, X.; Frandsen, W.; Wang, D.; Su, D. Hydrothermal synthesis of microscale boehmite and gamma nanoleaves alumina. *Mater. Lett.* **2008**, *62*, 1297–1301.
92. Yao, M.H.; Baird, R.J.; Kunz, F.W.; Hoost, T.E. An XRD and TEM investigation of the structure of alumina-supported ceria-zirconia. *J. Catal.* **2007**, *166*, 67–74.
93. Riguetto, B.A.; Damyanova, S.; Gouliev, G.; Marques, C.M.P.; Petrov, L.; Bueno, J.M.C. Surface behavior of alumina-supported Pt catalyst modified with cerium as revealed by X-ray Diffraction, X-RAY Photoelectron Spectroscopy, and Fourier Transform Infrared Spectroscopy of CO Adsorption. *J. Phys. Chem. B* **2004**, *108*, 5349–5358.
94. Adams, K.M.; Gandhi, H.S. Palladium-tungsten catalysts for automotive exhaust treatment. *Ind. Eng. Chem. Prod. Res. Dev.* **1983**, *22*, 207–212.
95. Torncrona, A.; Skoglundh, M.; Thormahlen, P.; Fridell, E.; Jobson, E. Low temperature catalytic activity of cobalt oxide and ceria promoted Pt and Pd: -Influence of pretreatment and gas composition. *Appl. Catal. B* **1997**, *14*, 131–146.
96. Canton, P.; Fagherazzi, G.; Battagliarin, M.; Menegazzo, F.; Pinna, F.; Pernicone, N. Pd/CO average chemisorption stoichiometry in highly dispersed supported $Pd/\gamma\text{-}Al_2O_3$ catalysts. *Langmuir* **2002**, *18*, 6530–6535.